



**HAL**  
open science

# Outage Probability Analysis of a Vertical Underwater Wireless Optical Link Subject to Oceanic Turbulence and Pointing Errors

Ikenna Chinazaekpere Ijeh, Mohammad Ali Khalighi, Mohammed Elamassie, Steve Hranilovic, Murat Uysal

► **To cite this version:**

Ikenna Chinazaekpere Ijeh, Mohammad Ali Khalighi, Mohammed Elamassie, Steve Hranilovic, Murat Uysal. Outage Probability Analysis of a Vertical Underwater Wireless Optical Link Subject to Oceanic Turbulence and Pointing Errors. *Journal of Optical Communications and Networking*, 2022, 14 (6), pp.439. 10.1364/JOCN.454191 . hal-03937222

**HAL Id: hal-03937222**

**<https://hal.science/hal-03937222>**

Submitted on 13 Jan 2023

**HAL** is a multi-disciplinary open access archive for the deposit and dissemination of scientific research documents, whether they are published or not. The documents may come from teaching and research institutions in France or abroad, or from public or private research centers.

L'archive ouverte pluridisciplinaire **HAL**, est destinée au dépôt et à la diffusion de documents scientifiques de niveau recherche, publiés ou non, émanant des établissements d'enseignement et de recherche français ou étrangers, des laboratoires publics ou privés.

# Outage Probability Analysis of a Vertical Underwater Wireless Optical Link Subject to Oceanic Turbulence and Pointing Errors

I. C. Ijeh<sup>1</sup>, M. A. Khalighi<sup>1</sup>, M. Elamassie<sup>3</sup>, S. Hranilovic<sup>2</sup>, M. Uysal<sup>3</sup>

<sup>1</sup>Aix Marseille University, CNRS, Centrale Marseille, Institut Fresnel, Marseille, France

<sup>2</sup>McMaster University, Dept. Electrical & Computer Engineering, Hamilton, ON, Canada

<sup>3</sup>Özyeğin University, Department of Electrical & Electronics Engineering, Istanbul, Turkey

**Abstract**—The reliability of an underwater wireless optical communication (UWOC) network is seriously impacted by beam misalignment between the transmitters (Tx) and the receivers (Rx). Also, the performance of UWOC systems can be affected by oceanic turbulence-induced fading due to fluctuations in the water refractive index as a result of variations in the pressure and water temperature and salinity. In this work, we investigate performance analysis of a vertical UWOC link subject to oceanic turbulence and pointing errors, and further investigate the appropriate selection of link parameters to optimize link performance. This study is based on an accurate mathematical framework for the link modeling while taking into account realistic Tx/Rx and channel parameters under different turbulence and beam misalignment conditions. Meanwhile, we provide an analytical expression for calculating the link outage probability, whose accuracy is validated through numerical simulations. Lastly, the necessity of optimal Tx/Rx parameter selection to minimize the link outage is demonstrated. A laser beam is considered at the Tx, as well as an ultra-sensitive photo-detector (silicon photo-multiplier) at the Rx in order to enable working at relatively long link ranges. The presented results give valuable insight to the practical aspects of deployment of UWOC networks.

**Index Terms**—Underwater wireless optical communications; pointing errors; oceanic turbulence; silicon photo-multiplier; aperture averaging; parameter optimization.

## I. INTRODUCTION

Today, demands for underwater communication networks are increasing due to the on-going expansion of the related human activities, such as environmental monitoring, offshore oil field exploration, port security, etc. Such networks should enable communication with underwater vehicles or to harvest data from underwater sensors. Within the paradigm of underwater Internet of things, we are concerned with diverse range and data-rate requirements and a challenging and unpredictable propagation environment. Within this context, underwater wireless optical communications (UWOC) are considered as an efficient complementary technology to acoustic communications for short-to-moderate link ranges, allowing for high-speed, low-latency data transmission in such networks [1, 2, 3]. In practice, the UWOC link performance is impacted by several parameters including water absorption and scattering [4, 5, 6], solar background noise [7, 8], oceanic turbulence

[9], and pointing errors (PEs) [10, 11, 12], thus necessitating efficient techniques for mitigating these effects. On the other hand, in order to increase link range, the use of highly sensitive photo-detectors (PD) at the receiver (Rx) has received particular attention, such as photo-multiplier tubes (PMTs), single-photon avalanche diodes (SPADs), and arrays of SPADs also known as silicon photo-multipliers (SiPMs) or multi-pixel photon counters (MPPCs) [13].

In this work, the focus is on the impacts of oceanic turbulence and PEs, which dominate the dynamic performance of underwater links. We further consider the appropriate selection of the transmitter (Tx)/Rx parameters to minimize the impact of random channel effects.

A number of recent works have investigated the effect of oceanic turbulence on the performance of UWOC links. In the case of oceanic turbulence, [14] carried-out experimental measurements focusing mainly on the index of refraction structure constant (representing the turbulence strength). In [15], the effect of turbulence on the Rx signal-to-noise ratio (SNR) was studied with varying Tx and Rx parameters. Taking into account air bubbles and the temperature gradient, [16] proposed a unified statistical model based on experimental data to characterize the turbulence. Also, in the case of a vertical UWOC link, [17] modeled the optical channel by several layers with uniform thickness but of different turbulent strengths. This approach recognizes that oceanic temperature and salinity profiles are not smooth functions of the depth but rather change in a nearly step-wise manner. In particular, weak gradient layers with thickness on the order of meters are separated by strong gradient sheets with thickness on the order of centimeters [18]. On the other hand, to reduce the effect of turbulence, aperture averaging was studied in [19] considering a Gaussian beam under weak turbulence conditions. Also, the reduction in the scintillation index by using adaptive optics and aperture averaging was studied in [20]. The effect of aperture averaging on the average link bit-error-rate (BER) for moderate to strong oceanic turbulence was investigated in [21].

Concerning the problem of link misalignment and PEs, [11] investigated the tolerable Rx offset distance to maintain a

reliable communication. Also, for a tolerable lateral offset between the Tx and the Rx, [22] studied the effect of the divergence angle of an optical beam on the received power. Considering a vertical UWOC system with the Tx located on the sea surface and the Rx underneath, [23] and [24] investigated the effect of angular misalignment of the optical beam axis on the link performance due to the roughness of the sea surface caused by wind speed. For relatively short link ranges, the use of angular multiple-input multiple-output (MIMO) technique was proposed in [12, 25], allowing increased robustness against PEs. In a recent work [26], we studied the effect of Tx-Rx parameter optimization on the performance of a vertical UWOC link subject to PEs.

In this paper, the performance of a vertical link subject to turbulence, PEs, and solar background noise is studied based on accurate mathematical modeling and analytical expression of the link outage probability. More specifically, in the considered application scenario, the communication takes place vertically, between a surface unit, which can take the form of a buoy, an autonomous surface vehicle (ASV), or a boat, and an autonomous underwater vehicle (AUV), an underwater drone or an underwater sensor node beneath it [27, 28]. Typically, the surface unit can serve as a relay node for long-range data transmission from/to a ground station or a satellite [29]. The underwater link can involve data upload from the sensor node or the underwater unit to the relay node, or data download from the relay node to the underwater unit for the purposes of control/command or sending localization data, etc.

A typical scenario of buoy-to-AUV downlink data transmission is illustrated in Fig. 1, where the deviations in the orientation and the position of the buoy with respect to the AUV can affect the link reliability. To increase link range, we consider the use of an SiPM at the Rx, which offers a very high internal gain, together with the ease of implementation and mechanical robustness, as compared to PMT-based Rx's [13, 30, 31].

In contrast to our previous work in [26], here we take into account the effects of turbulence and solar background noise, as well as using a laser diode (LD) at the Tx (instead of an LED source, as considered in [26]). Using a laser source results in a higher modulation bandwidth and a higher beam directivity. We present an accurate statistical model for the channel turbulence that takes into account the aperture averaging effect, which, to the best of the authors' knowledge, has not been considered in the literature so far for the case of an inhomogeneous vertical link. Moreover, we provide a closed-form expression for the link outage probability and further show the improvement in the link performance by appropriate selection of the Tx/Rx parameters, i.e., the Tx beam width and the Rx aperture size and field-of-view (FoV).

The remainder of the paper is organized as follows. Section II introduces the main assumptions of the considered system and the formulation of the link performance metric. Next, Section III focuses on channel modelling, taking into account attenuation, turbulence, and PEs and the derivation of outage

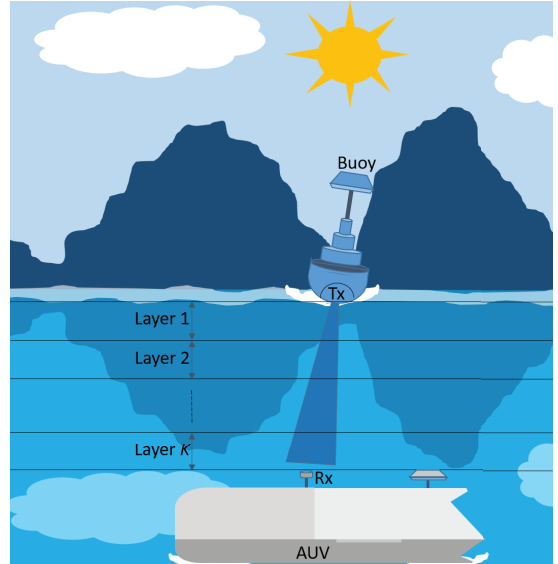


Fig. 1: Illustration of a typical Buoy-AUV vertical UWOC link scenario, considered in the paper.

probability expressions is presented in Section IV. Afterwards, Section V investigates the random channel effects on the link performance and the interest of optimized Tx/Rx parameter selection. Lastly, Section VI concludes the paper and outlines some future research directions.

*Notation:* Probability is denoted by  $\Pr(\cdot)$ ;  $\delta(\cdot)$  stands for the Dirac delta function;  $E\{\cdot\}$  denotes the expected value;  $\|\cdot\|^2$  stands for vector norm;  $\text{erfc}(x) = \frac{2}{\sqrt{\pi}} \int_x^\infty e^{-t^2} dt$  is the complementary error function; and  $\mathcal{N}(\mu, \sigma^2)$  denotes a Gaussian distribution of mean  $\mu$  and variance  $\sigma^2$ .

## II. MAIN ASSUMPTIONS AND SIGNAL TRANSMISSION FORMULATION

Fig. 2 shows the block diagram of the UWOC system based on intensity modulation and direct detection (IM/DD). The optical source is a LD, assumed to have a Gaussian beam profile [32]. The transmission range is denoted by  $L$  and the Rx lens diameter by  $D_r$ . An optical filter is also typically used in order to reduce the received background noise level.

Let  $h$  denote the channel coefficient, which includes the effects of propagation loss (due to absorption and scattering), turbulence, and Tx-Rx random misalignment. Signal modulation is based on non-return to zero (NRZ) on-off keying (OOK), and a frequency non-selective channel is assumed.<sup>1</sup> The generated photo-current at the SiPM output passes through a transimpedance amplifier (TIA) and then a low-pass filter (LPF) to limit the Rx noise. For the transmitted OOK signal  $s_i$ ,  $i \in \{0, 1\}$ , two intensity values of  $P_{Tx_0}$  and  $P_{Tx_1}$  are used, corresponding to OFF and ON states, respectively, with the average transmit optical power of  $P_{Tx}$  and the extinction ratio

<sup>1</sup>Higher spectral efficiency signaling schemes or alternatively, channel equalization at the Rx may be used to increase the data rate over the system bandwidth limitation [30, 33].

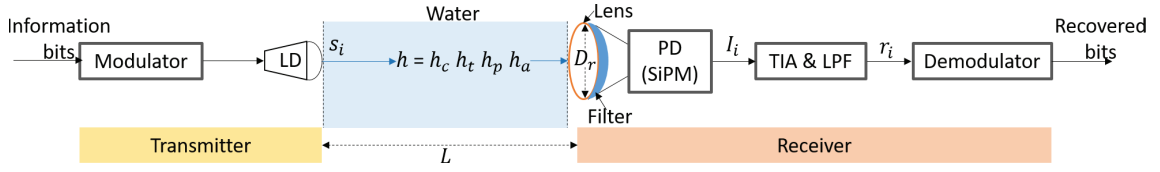


Fig. 2: The block diagram of the UWOC communication link.

$\xi = P_{Tx0}/P_{Tx1}$ . The average received power  $P_{Rx}$  at the Rx lens is  $P_{Rx} = h P_{Tx}$ , and the generated photo-current  $I_i$  at the SiPM output is

$$I_i = \underbrace{\mathcal{R}_e s_i h}_{I_{s,i}} + I_d + I_b + n_{s_i} = \check{I}_i + n_{s_i}, \quad (1)$$

where  $I_{s,i}$ ,  $I_d$ , and  $I_b$  represent the useful signal, the dark current, and the photo-current due to background radiations; and  $n_{s_i}$  is the Rx noise, including shot noise and the random components of dark and background noises. Also,  $\mathcal{R}_e$  is the SiPM responsivity, given by [31]

$$\mathcal{R}_e = \left( \frac{\Upsilon_{PDE}}{E_{ph}} \right) (1 + P_{AP} + P_{CT}) e G. \quad (2)$$

Here,  $\Upsilon_{PDE}$  is the photon detection efficiency, and  $P_{AP}$ ,  $P_{CT}$ ,  $E_{ph}$ ,  $e$ , and  $G$  denote the probability of after-pulsing, probability of cross-talk, the photon energy, electron charge, and SiPM gain, respectively. Note that, in general, the PD responsivity is a function of wavelength. Here, due to the use of the narrow optical filter, the considered  $\mathcal{R}_e$  corresponds to the LD wavelength. The SiPM dark current is

$$I_d = f_{DCR} (1 + P_{AP} + P_{CT}) e G, \quad (3)$$

where  $f_{DCR}$  is the dark count rate [31]. Considering the background noise optical power  $P_b$  due to solar radiation captured at the Rx, the subsequently generated current is expressed as [7]

$$I_b = \mathcal{R}_e \underbrace{E_{sun}(\lambda, L) \pi \theta_{FoV}^2 T_w T_f B_o (\pi D_r^2 / 4)}_{P_b}, \quad (4)$$

where  $T_w$  is the water transmittance,  $B_o$  and  $T_f$  are the bandwidth and the transmittance of the Rx optical filter, respectively, and  $\theta_{FoV}$  denotes the Rx FoV in radians. Also,  $E_{sun}(\lambda, L) = E_{sun}(\lambda, 0) e^{-(L K_d)}$  is the down-welling spectral irradiance of the solar noise at wavelength  $\lambda$ , with  $E_{sun}(\lambda, 0)$  as at the sea surface. This approximate exponential attenuation model, accounting for absorption and scattering, applies to a diffused source (here, the solar radiation) and relatively low-turbidity waters [7, 34]. The so-called diffuse attenuation coefficient  $K_d$  depends on the depth, the wavelength, and the concentration of particles in water.<sup>2</sup>

The voltage signal at the LPF output is given by

$$r_i = R_L I_i + n_{th} = \underbrace{R_L \check{I}_i}_{\check{r}_i} + R_L n_{s_i} + n_{th}, \quad (5)$$

<sup>2</sup>Since the variations of  $K_d$  are relatively small in the blue-green part of the spectrum [35], we assume for simplicity that  $K_d$  is nearly fixed.

where  $R_L$  is the load resistance of the TIA and  $n_{th}$  is the thermal noise with variance  $\sigma_{th}^2$ . The total Rx noise, which is signal-dependent, is modeled as a zero mean Gaussian noise with variance  $\sigma_{n_i}^2$

$$\begin{aligned} \sigma_{n_i}^2 &= R_L^2 \sigma_{n_{s_i}}^2 + \sigma_{th}^2 \\ &= R_L^2 (\sigma_{sh,i}^2 + \sigma_d^2 + \sigma_b^2) + \sigma_{th}^2, \end{aligned} \quad (6)$$

where  $\sigma_{sh,i}^2$ ,  $\sigma_d^2$ , and  $\sigma_b^2$  denote the variances of the signal shot noise, dark noise, and background noise, respectively. We have

$$\begin{cases} \sigma_{sh,i}^2 &= 2 e G F B_e I_{s,i}, \\ \sigma_d^2 &= 2 e G F B_e I_d, \\ \sigma_b^2 &= 2 e G F B_e I_b, \\ \sigma_{th}^2 &= 4 K_Z T_e B_e R_L. \end{cases} \quad (7)$$

Here,  $K_Z$ ,  $T_e$ ,  $F$ , and  $B_e$  denote the Boltzmann constant, the Rx equivalent temperature in Kelvin, the PD excess noise factor, and the bandwidth of the Rx LPF, respectively. Here,  $B_e \approx R_b/2$ , with  $R_b$  being the bit rate with NRZ OOK modulation without considering any forward error correction [36].

Assume that the Rx has perfect knowledge of  $h$ , based on which the optimal OOK demodulation threshold  $\gamma_{th}$  can be calculated. Taking into account the signal-dependent Rx noise, the instantaneous BER  $P_e(e|h)$  can be expressed as [37]

$$P_e(e|h) = \frac{1}{4} \operatorname{erfc} \left( \frac{\gamma_{th} - \check{r}_0}{\sqrt{2} \sigma_{n_0}} \right) + \frac{1}{4} \operatorname{erfc} \left( \frac{\check{r}_1 - \gamma_{th}}{\sqrt{2} \sigma_{n_1}} \right), \quad (8)$$

where  $\check{r}_0$  and  $\check{r}_1$  stand for the signal parts of the demodulator input for bits '0' and '1', respectively (see (5)), and  $\sigma_{n_0}^2$  and  $\sigma_{n_1}^2$  denote the corresponding noise variances, calculated from (6). We have [37]

$$\begin{aligned} \gamma_{th} &= \frac{\check{r}_0 \sigma_{n_1}^2 - \check{r}_1 \sigma_{n_0}^2}{\sigma_{n_1}^2 - \sigma_{n_0}^2} + \left[ \frac{\check{r}_1^2 \sigma_{n_0}^2}{\sigma_{n_1}^2 - \sigma_{n_0}^2} + \right. \\ &\quad \left. \left( \frac{\check{r}_0 \sigma_{n_1}^2 - \check{r}_1 \sigma_{n_0}^2}{\sigma_{n_1}^2 - \sigma_{n_0}^2} \right)^2 - \frac{\check{r}_0^2 \sigma_{n_1}^2}{\sigma_{n_1}^2 - \sigma_{n_0}^2} \right. \\ &\quad \left. - \frac{\sigma_{n_0}^2 \sigma_{n_1}^2}{\sigma_{n_1}^2 - \sigma_{n_0}^2} \ln \left( \frac{\sigma_{n_0}^2}{\sigma_{n_1}^2} \right) \right]^{0.5}. \end{aligned} \quad (9)$$

Then, the average BER is then given by

$$P_e = \int_0^\infty P_e(e|h) f_h(h) dh, \quad (10)$$

where  $f_h(h)$  is the probability density function (PDF) of  $h$ . Given the relatively slow channel time variations (due to either PEs or turbulence), the outage probability  $P_{out}$  is a more

appropriate metric for evaluating the link performance, that we consider here. It is defined as the probability of the instantaneous BER exceeding a threshold  $\text{BER}_{\text{th}}$ , or equivalently, the probability of  $h$  being smaller than a threshold  $h_{\text{th}}$

$$P_{\text{out}} = \Pr(h < h_{\text{th}}) = \int_0^{h_{\text{th}}} f_h(h) dh. \quad (11)$$

The analytical expression of  $h_{\text{th}}$  and the explanation of its derivation are provided in Appendix A.

### III. CHANNEL MODEL

For the considered vertical UWOC system, the channel coefficient  $h$  is modeled as

$$h = h_c h_t h_p h_a, \quad (12)$$

where  $h_c$  denotes the propagation loss, which is the deterministic part of  $h$ , while the random components  $h_t$ ,  $h_p$ , and  $h_a$  represent the effects of turbulence, pointing errors, and link interruption, respectively.

#### A. Propagation Loss

The factor  $h_c$  represents the attenuation in signal intensity as a result of absorption and scattering. Here, to simplify the derivation of analytical models for the link performance metrics, we approximate  $h_c$  by the exponential attenuation model of Beer-Lambert, which neglects the multiple scattering effect [4, 6]

$$h_c = \exp(-L c_e), \quad (13)$$

where  $c_e$  denotes the beam extinction coefficient for a collimated light source, e.g., a laser beam, in contrast to  $K_d$  which is considered for a diffuse light source [38].

#### B. Oceanic Turbulence

Oceanic turbulence is as a result of random variations of the refractive index along the aquatic medium, which causes fluctuations in both intensity and phase of the average received signal [39]. For a vertical UWOC link, these fluctuations are mostly due to the variations in the water temperature and salinity with depth. Based on the profiles of temperature and salinity in the Argo database [40] for different geographical locations and over a long period of time, the log-normal PDF shows a good match with the majority of measured temperature and salinity gradients [41]. We, hence, model  $h_t$  by a log-normal distribution, that is,

$$h_t = \exp(T), \quad (14)$$

where  $T$  denotes the log-amplitude coefficient of turbulence, following the Gaussian distribution  $\mathcal{N}(\mu_T, \sigma_T^2)$ . The PDF of  $h_t$  is

$$f_{h_t}(h_t) = \frac{1}{h_t \sqrt{2\pi\sigma_T^2}} \exp\left(-\frac{(\ln(h_t) - \mu_T)^2}{2\sigma_T^2}\right). \quad (15)$$

Note that other models have been proposed for the cases of moderate-to-strong turbulence, e.g., the Gamma-Gamma PDF in [17].

Following the approach in [17], and as illustrated in Fig. 3, the channel is considered as a cascade of layers with different mean and variance turbulence parameters, where they are assumed as unchanged within each layer. Assume a total of  $K$  layers, with the  $k^{\text{th}}$  layer of thickness  $L_k$  (where  $L = \sum_{k=1}^K L_k$ ), mean  $\mu_{T_k}$ , and variance  $\sigma_{T_k}^2$ . The PDF of the corresponding channel coefficient  $h_{tk}$  is

$$f_{h_{tk}}(h_{tk}) = \frac{1}{h_{tk} \sqrt{2\pi(4\sigma_{T_k}^2)}} \exp\left(-\frac{(\ln(h_{tk}) - 2\mu_{T_k})^2}{2(4\sigma_{T_k}^2)}\right). \quad (16)$$

The relationship between  $\sigma_{T_k}^2$  and the scintillation index of  $k^{\text{th}}$  layer  $\sigma_{I_k}^2$  is given by [42]

$$\sigma_{T_k}^2 = 0.25 \ln(1 + \sigma_{I_k}^2) \approx 0.25 \sigma_{I_k}^2 \text{ for } \sigma_{I_k}^2 \ll 1. \quad (17)$$

Note that this relationship is valid for the weak turbulence regime, i.e., for  $\sigma_{I_k}^2 < 1$ . Assuming independent, non-identically distributed  $h_{tk}$ ,  $\mu_T$  and  $\sigma_T^2$  in (15) are [17]

$$\begin{cases} \mu_T &= \sum_{k=1}^K 2\mu_{T_k}, \\ \sigma_T^2 &= \sum_{k=1}^K 4\sigma_{T_k}^2. \end{cases} \quad (18)$$

To normalize the fading coefficient, i.e., to have  $\text{E}\{h_{tk}\} = 1$ , we set  $\mu_{T_k} = -\sigma_{T_k}^2$ .

A well-known method to reduce the scintillation effect on the received signal is aperture averaging, by using a Rx aperture diameter  $D_r$  larger than the correlation width of the irradiance fluctuations  $\rho_c$  [43]. For a horizontal link, and under weak turbulence conditions, the correlation width for a Gaussian beam is given by  $\rho_c \sim \sqrt{L/\mathcal{K}}$ , where  $\mathcal{K} = 2\pi/\lambda$  is the wave number. The effect of aperture averaging has been studied in a few previous works for horizontal UWOC links [19, 20, 21]. To investigate the efficiency of aperture averaging in reducing the oceanic turbulence effect in the considered application scenario, we assume that the Rx uses a Gaussian lens, which is a combination of a thin lens with a Gaussian limiting aperture (i.e., a *soft* aperture) [32].

Assuming a large enough photo-detector active area [43], to obtain the PDF of (15) while accounting for aperture averaging, first the scintillation indexes  $\sigma_{I_k}^2(D_r)$  corresponding to each of the  $k^{\text{th}}$ -layer should be calculated, see (43) in Appendix A, which is then used in (17) to obtain  $\sigma_{T_k}^2$ . This latter is then used in (18) to calculate the PDF parameters  $\mu_T$  and  $\sigma_T^2$ .

#### C. Pointing Errors

Considering the buoy-to-AUV UWOC link, the beam alignment is affected due to the sea surface waves, underwater currents, and the instability of both the Tx and the Rx platforms. As a result, the center of the beam spot (with maximum signal intensity) at the Rx deviates from the center of the Rx aperture.

This is illustrated together with the perfect alignment case in Fig. 3, which shows the angular misalignment of the Tx and the Rx, denoted by  $\theta_{tx}$  and  $\theta_{rx}$ , as well as the displacement of the Rx with respect to the Tx position in  $(x, y)$  plane. The instantaneous Cartesian coordinates of the Tx and the Rx are denoted by  $[x_t, y_t, z_t]$  and  $[x_r, y_r, z_r]$ , respectively. We set  $z_t = 0$ , then  $z_r = L$ . For the misaligned case, angles  $\theta_{tx}$  and  $\theta_{rx}$  denote the Tx and Rx angular misalignment in  $(x, z)$  Cartesian coordinates. Also, angles  $\phi_{tx}$  and  $\phi_{rx}$  are

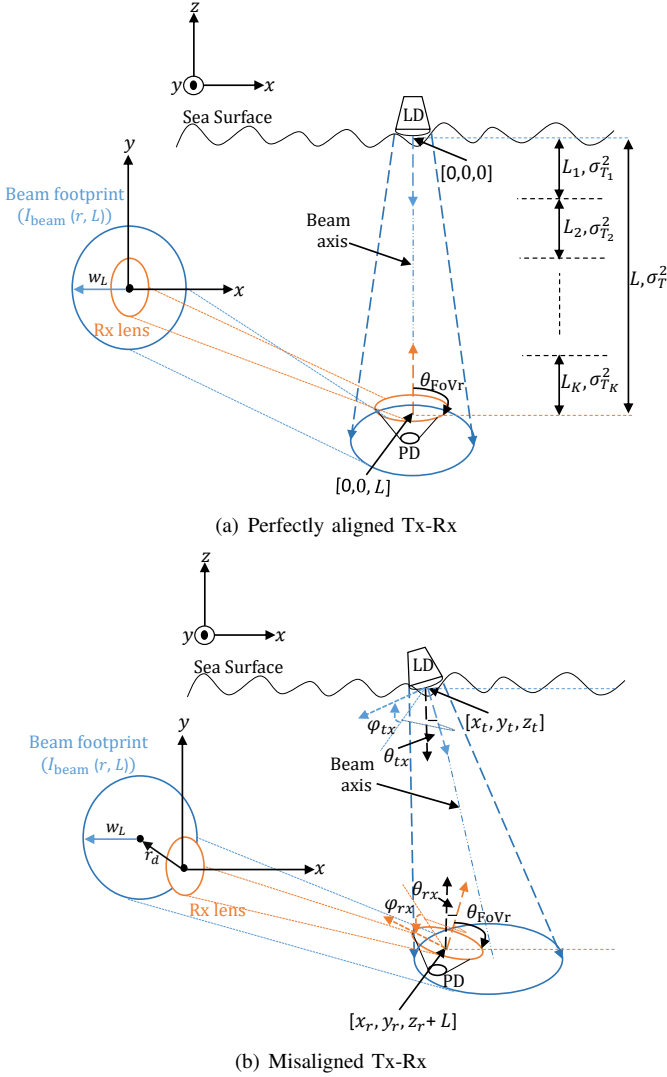


Fig. 3: Geometry of the buoy-AUV UWOC downlink, for the cases of (a) perfectly aligned and (b) misaligned Tx/Rx highlighting angular misalignment and displacement. The top view of the Rx plane (the Rx lens and the beam footprint with radius  $w_L$ ) is detailed at left, whereas the layered turbulence modeling is shown at right in (a).

approximately equal to  $x_t/L$  and  $x_r/L$ , respectively, assuming  $L$  to be very large compared to the other Tx-Rx coordinates. Note that the corresponding misalignment angles  $\theta_{ty}$ ,  $\phi_{ty}$ ,  $\theta_{ry}$ , and  $\phi_{ry}$  in  $(y, z)$  coordinates are not illustrated. For the sake of simplicity, we assume a circular beam spot at the PD for the case of angular misalignment. Note that a more accurate

modeling should consider an elliptical shape of the beam as in [44].

We assume that the Rx lateral displacement with respect to the Tx is much smaller than the operation depth  $L$  (see Subsection V-A), thus the link range  $Z$  is approximately equal to  $L$ . Considering a Gaussian beam at the Tx, the normalized spatial distribution of the irradiance at distance  $L$  is given by [45]

$$I_{\text{beam}}(r, L) = \frac{2}{\pi w_L^2} \exp\left(-\frac{2\|r\|^2}{w_L^2}\right), \quad (19)$$

where  $r = [x, y]$  is the radial vector from the beam center and  $w_L$  is the beam waist at distance  $L$ .<sup>3</sup>

Under perfect Tx-Rx alignment conditions, the normal of the Tx and the Rx are on their respective  $z$ -axis. For the beam misalignment case, the Tx and the Rx angular misalignment ( $\theta_{tx}$ ,  $\theta_{ty}$ ,  $\theta_{rx}$ ,  $\theta_{ry}$ ), and displacements ( $x_t$ ,  $y_t$ ,  $x_r$ ,  $y_r$ ), are for simplicity modeled as zero mean Gaussian distribution<sup>4</sup> with their respective variance as  $(\sigma_{\theta_t}^2, \sigma_{\theta_r}^2)$  and  $(\sigma_{pt}^2, \sigma_{pr}^2)$ .

Considering the orientation of the Tx and the positions of the Tx and the Rx, the deviation of the transmitted beam spot from the center of the Rx aperture can be expressed as [46]

$$r_d = \sqrt{x_d^2 + y_d^2}, \quad (20)$$

where,

$$x_d = x_t + x_r + Z \tan(\theta_{tx}) \quad (21)$$

$$y_d = y_t + y_r + Z \tan(\theta_{ty}). \quad (22)$$

Here, as mentioned previously, we approximate  $Z \approx L$  for simplicity. The PE loss coefficient is given by [47]

$$h_p \approx A_0 \exp\left(-\frac{2r_d^2}{w_{Leq}^2}\right), \quad (23)$$

where  $A_0 = (\text{erf}(\nu))^2$  stands for the maximum fraction of received power, corresponding to  $r_d = 0$  with  $\nu = (D_r \sqrt{\pi}) / (2\sqrt{2}w_L)$ . Also,  $w_{Leq}$  is the equivalent beam width at the Rx

$$w_{Leq} = \sqrt{w_L^2 \frac{\sqrt{\pi} \text{erf}(\nu)}{2\nu \exp(-\nu^2)}} \quad (24)$$

The cumulative distribution function (CDF) of  $h_p$  is

$$\begin{aligned} F_{h_p}(h_p) &= \Pr\left(A_0 \exp\left(-\frac{2r_d^2}{w_{Leq}^2}\right) \leq h_p\right) \\ &= \Pr\left(r_d > \sqrt{-\frac{w_{Leq}^2}{2} \ln\left(\frac{h_p}{A_0}\right)}\right) \\ &= 1 - F_{r_d}\left(\sqrt{-\frac{w_{Leq}^2}{2} \ln\left(\frac{h_p}{A_0}\right)}\right), \end{aligned} \quad (25)$$

<sup>3</sup>Note that  $w_L$  can approximately be expressed as the product of the LD divergence angle at  $1/e^2$  of the maximum irradiance,  $\theta_0$  (in rad), and the link range  $L$ , i.e.,  $w_L \approx \theta_0 L$ .

<sup>4</sup>Note that, in contrast with our previous work in [26] where a dedicated PDF was considered for  $\theta_{tx}$ , which only took into account the wind sea surface within a very limited range (obtained based on experimental measurements), here we consider the general model of a Gaussian distributed  $\theta_{tx}$ .

where  $F_{r_d}(r_d)$  denotes the CDF of  $r_d$ . Differentiating (25) with respect to  $h_p$  gives the PDF as

$$f_{h_p}(h_p) = \frac{w_{Leq}^2}{4h_p \sqrt{-\frac{w_{Leq}^2}{2} \ln\left(\frac{h_p}{A_0}\right)}} f_{r_d}\left(\sqrt{-\frac{w_{Leq}^2}{2} \ln\left(\frac{h_p}{A_0}\right)}\right), \quad (26)$$

where  $f_{r_d}(\cdot)$  is the PDF of  $r_d$ , which based on the prior assumptions, follows a Rayleigh distribution

$$f_{r_d}(r_d) = (r_d/\sigma_{r_d}^2) \exp(-r_d^2/2\sigma_{r_d}^2), \quad (27)$$

with  $\sigma_{r_d}^2$  denoting the jitter variance.

#### D. Link interruption

The last factor in (12) is the link interruption  $h_a$ , which takes the values 0 or 1 depending on whether or not the angle-of-arrival (AoA)  $\theta_a$  of the receiving beam is outside or inside the Rx FoV. In other words,  $h_a = \Pi(\theta_a/\theta_{\text{FoVr}})$ , where  $\Pi(x) = 1$  if  $|x| \leq 1$ , and zero, otherwise. Also [46],

$$\theta_a = \tan^{-1}\left(\sqrt{(\tan(\theta_{tx} + \theta_{rx}))^2 + (\tan(\theta_{ty} + \theta_{ry}))^2}\right), \quad (28)$$

with the PDF as

$$f_{\theta_a}(\theta_a) = \frac{\theta_a}{\sigma_{\theta_t}^2 + \sigma_{\theta_r}^2} \exp\left(-\frac{\theta_a^2}{2(\sigma_{\theta_t}^2 + \sigma_{\theta_r}^2)}\right). \quad (29)$$

Then, the PDF of  $h_a$  can be expressed as [46]

$$f_{h_a}(h_a) = F_{\theta_a}(\theta_{\text{FoVr}}) \delta(h_a - 1) + (1 - F_{\theta_a}(\theta_{\text{FoVr}})) \delta(h_a), \quad (30)$$

where  $F_{\theta_a}(\theta_a)$  is the CDF of  $\theta_a$ , and  $F_{\theta_a}(\theta_{\text{FoVr}})$  denotes the probability that the AoA falls within the Rx FoV

$$F_{\theta_a}(\theta_{\text{FoVr}}) = \int_0^{\theta_{\text{FoVr}}} f_{\theta_a}(\theta_a) d\theta_a = 1 - \exp\left(-\frac{\theta_{\text{FoVr}}^2}{2(\sigma_{\theta_t}^2 + \sigma_{\theta_r}^2)}\right). \quad (31)$$

#### IV. OUTAGE PERFORMANCE EVALUATION

Considering the various channel effects and denoting  $h' = h_c h_t h_p$ , the PDF of  $h = h' h_a$  can be expressed as

$$f_h(h) = \int_0^\infty f_{h'}(h') f_{h|h'}(h|h') dh', \quad (32)$$

$$f_{h|h'}(h|h') = \frac{1}{h'} f_{h_a}\left(\frac{h}{h'}\right). \quad (33)$$

Replacing (33) in (32),  $f_h(h)$  can be written as in (34) on the top of the next page, where  $f_h(h > 0)$  and  $f_h(h = 0)$  denote the occurrence or not of link interruption in  $f_h(h)$ , respectively.

To evaluate the link performance, the link outage probability  $P_{\text{out}}$  can be calculated using (34) in (11). After some mathematical manipulations explained in Appendix A, the closed form asymptotic expression of (35) is obtained, which is valid for small  $P_{\text{out}}$ , i.e., for  $h_{\text{th}} \rightarrow 0$ .

Let us for the sake of completeness consider the special case of a large Rx FoV, where no link interruption occurs. In this case, we have  $h = h_c h_t h_p$  with  $f_h(h)$  as

$$f_h(h) = \int_0^\infty f_{h_t}(h_t) f_{h|h_t}(h|h_t) dh_t, \quad (36)$$

where,

$$f_{h|h_t}(h|h_t) = \frac{1}{h_c h_t} f_{h_p}\left(\frac{h}{h_c h_t}\right). \quad (37)$$

Then, it can be shown that

$$\lim_{h_{\text{th}} \rightarrow 0} P_{\text{out}} = (A_0 h_c)^{-\frac{w_{Leq}^2}{4\sigma_{r_d}^2}} \exp\left(-\mu_T \frac{w_{Leq}^2}{4\sigma_{r_d}^2}\right) \times \exp\left(\sigma_T^2 \frac{w_{Leq}^4}{32\sigma_{r_d}^4}\right) h_{\text{th}}^{\frac{w_{Leq}^2}{4\sigma_{r_d}^2}}. \quad (38)$$

We will refer to (35) and (38) as upper bounds on  $P_{\text{out}}$ . We will show later in Section V that these upper bounds are tight enough, and therefore quite useful for system design, in particular for low solar noise levels.

#### V. NUMERICAL RESULTS

This section presents numerical results to study the performance of the considered UWOC link under different conditions of solar noise, turbulence, and PEs. We will also consider the optimal selection of the Tx/Rx parameters to minimize the link outage.<sup>5</sup>

##### A. Specification of Underwater Scenario and Link Parameters

We consider an UWOC system operating in Pacific Ocean of high latitudes, where the variations in the salinity and temperature with depth can be approximately considered as being step-like, i.e., corresponding to non-mixing layers [48]. This choice is due to the availability of data for realistic turbulence modeling; the corresponding temperature and salinity profiles are given in Fig. 4 [17, 48] and used to calculate the scintillation index and the turbulence power spectrum (given by (43) and (45) in Appendix A, respectively). We assume the case of clear ocean waters with the typical chlorophyll concentration of  $C_{cl} = 0.5 \text{ mg/m}^3$ , which corresponds to  $K_d \approx 0.08 \text{ m}^{-1}$  and  $c_e \approx 0.151 \text{ m}^{-1}$ , and the water transmittance  $T_w \approx 0.97$  [34]. At the Tx, a LD on wavelength  $\lambda = 450 \text{ nm}$  with spectral width of  $\Delta\lambda = 2 \text{ nm}$ , and a Gaussian beam profile is considered with source size  $\alpha_s = 20 \text{ mm}$ , corresponding to the beam waist  $w_0 = \alpha_s \sqrt{2}$  (at source plane) [32]. The

<sup>5</sup>Note that in all the presented results, the downlink scenario, shown in Fig. 1, is considered.

$$\begin{aligned}
f_h(h) &= \int_0^\infty f_{h'}(h') \frac{1}{h'} \left[ F_{\theta_a}(\theta_{\text{FoVr}}) \delta\left(\frac{h-h'}{h'}\right) + (1 - F_{\theta_a}(\theta_{\text{FoVr}})) \delta\left(\frac{h}{h'}\right) \right] dh' \\
&= \int_0^\infty f_{h'}(h') \left[ F_{\theta_a}(\theta_{\text{FoVr}}) \delta(h-h') + (1 - F_{\theta_a}(\theta_{\text{FoVr}})) \delta(h) \right] dh' \\
&= \underbrace{f_{h'}(h) F_{\theta_a}(\theta_{\text{FoVr}})}_{f_h(h > 0)} + \underbrace{(1 - F_{\theta_a}(\theta_{\text{FoVr}})) \delta(h)}_{f_h(h = 0)},
\end{aligned} \tag{34}$$

$$\lim_{h_{\text{th}} \rightarrow 0} P_{\text{out}} = (A_0 h_c)^{-\frac{w_{Leq}^2}{4\sigma_{r_d}^2}} \exp\left(-\mu_T \frac{w_{Leq}^2}{4\sigma_{r_d}^2}\right) \exp\left(\sigma_T^2 \frac{w_{Leq}^4}{32\sigma_{r_d}^4}\right) h_{\text{th}}^{\frac{w_{Leq}^2}{4\sigma_{r_d}^2}} F_{\theta_a}(\theta_{\text{FoVr}}) + (1 - F_{\theta_a}(\theta_{\text{FoVr}})). \tag{35}$$

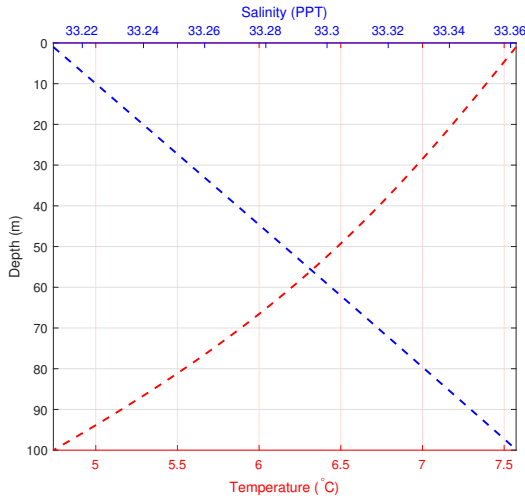


Fig. 4: Average temperature and salinity water profiles based on the measurements presented in [48]. Extraction was done following the approach in [17]. PPT stands for “Parts Per Thousand.”

LD peak output power  $P_{\text{Tx},1}$  is set depending on the link range; two values of 0.1 and 4W are considered here, the latter being considered as the default value.<sup>6</sup> At the Rx, an optical filter with bandwidth  $B_o = 2$  nm is used (the same as the LD spectral width), with transmittance  $T_f \approx 1$ , and a blue-sensitive SiPM (Reference SensL B-series MicroSB 30020 [51]). The link range, i.e., the AUV depth is considered to be  $L = 80$  m with  $w_L = 4$  m. For turbulence modeling, a 4-layer segmented vertical link is considered, assuming negligible change in the log-amplitude variance within a thickness of 20 m. Note that it has been shown in [52, 17] that there are negligible variations of temperature and salinity of seawater across a thickness of not more than 30 m.

Unless otherwise specified, a Rx aperture diameter of  $D_r = 75$  mm with a corresponding log-amplitude turbulence standard deviation of  $\sigma_T(D_r) = 0.0012$  at  $L = 80$  m is considered. Also, concerning PE parameters, i.e.,  $\sigma_{\theta_t}$ ,  $\sigma_{\theta_r}$ ,  $\sigma_{pt}$ , and  $\sigma_{pr}$ , we consider them as corresponding to the residual

<sup>6</sup>Note that, for instance, the MC100 modem from Shimadzu Co. uses blue LDs with optical output power up to a few watts [49]. Practically this can be achieved by combining various LDs using a fiber combiner [50].

deviations in the orientation and the position of a stable UWOC system. Then,  $\sigma_{\theta_t}$  and  $\sigma_{\theta_r}$  are typically on the order of a few tenths of degrees to a few degrees, and  $\sigma_{pt}$  and  $\sigma_{pr}$  on the order of a few tens of centimeters to a few meters.<sup>7</sup> We will consider by default  $\sigma_{\theta_t} = 0.1^\circ - 1^\circ$ ,  $\sigma_{\theta_r} = 0.1^\circ$ ,  $\sigma_{pt} = 1$  m, and  $\sigma_{pr} = 1$  m, unless otherwise specified.

Lastly, OOK signaling with extinction ratio of  $\xi = 0.4$  and bit rate of  $R_b = 1$  Mbps is considered. Also, the target BER is considered as the forward error correction threshold, i.e.,  $\text{BER}_{\text{th}} = 2 \times 10^{-3}$ . Tables I(a)-I(c) summarize the considered parameters.

### B. Effect of turbulence and aperture averaging

To assess the benefit of aperture averaging in reducing the turbulence effect, we have presented in Fig. 5 plots of the log-amplitude variance  $\sigma_T^2$  and the scintillation index  $\sigma_I^2$  versus  $D_r$  considering the absence of background noise and perfect beam alignment. Note that the considered minimum value of  $D_r$  corresponds to the PD size, i.e., without using a Rx lens. It can be seen that whereas the turbulence effect is quite important when the PD is directly used at the Rx, in the case of using a lens the turbulence strength is severely reduced thanks to aperture averaging. For instance, for  $D_r = 35$  and 75 mm,  $\sigma_I^2(D_r)$  is about  $2.7 \times 10^{-3}$  and  $6 \times 10^{-6}$ , respectively. So, even for a relatively small aperture size  $D_r$  of 35 mm, the impact of the turbulence is small and can be neglected. This can further be verified by evaluating the link  $P_{\text{out}}$  which almost equals zero for  $D_r \gtrsim 45$  mm (results are not shown). Lastly, for the considered  $D_r = 75$  mm, the log-amplitude variances and scintillation indexes of the underlying layers are  $\sigma_{T_1}^2 = 1.1 \times 10^{-7}$ ,  $\sigma_{T_2}^2 = 9.9 \times 10^{-8}$ ,  $\sigma_{T_3}^2 = 8.9 \times 10^{-8}$ ,  $\sigma_{T_4}^2 = 7.8 \times 10^{-8}$ , and  $\sigma_{I_1}^2 = 4.3 \times 10^{-7}$ ,  $\sigma_{I_2}^2 = 4 \times 10^{-7}$ ,  $\sigma_{I_3}^2 = 3.6 \times 10^{-7}$ ,  $\sigma_{I_4}^2 = 3.1 \times 10^{-7}$ .

<sup>7</sup>To provide a rough idea of the orientation and positioning accuracy in practice, consider, for instance, the Subsonus ultra-short baseline (USBL) acoustic positioning system [53]: For this product, the orientation accuracy of the transceiver (which could be at the buoy side) is about  $0.1^\circ$ , while the position accuracy of both the transceiver and transponder (the latter could be at the AUV side in our scenario) are about 0.1 and 0.25 m, respectively [53].



TABLE I: Tx-Rx and Channel Parameters

(a) Tx Parameters

Parameter	Value
LD wavelength $\lambda$	450 nm
LD spectral width $\Delta\lambda$	2 nm
LD peak transmit power $P_{Tx,1}$	4 W
OOK extinction ratio $\xi$	0.4
Bit rate $R_b$	1 Mbps

(b) Channel Parameters (used for turbulence modeling, see Appendix A)

Parameter	Value
Dissipation rate of mean-squared temperature $\mathcal{X}_T$	$10^{-5} \text{ K}^2 \text{ s}^{-1}$
Dissipation rate of turbulent kinetic energy, per unit mass of fluid $\epsilon$	$10^{-1} \text{ m}^2 \text{ s}^{-3}$
Thermal expansion coefficient $\alpha_k$	Computed by TEOS <sup>1</sup>
Saline contraction coefficient $\beta_k$	Computed by TEOS
Kinematic viscosity [28] $\nu_k$	Computed by FVCOM <sup>2</sup>
Molecular thermal diffusivity $D_{T_k}$	Computed by FVCOM
Molecular salinity diffusivity $D_{S_k}$	$D_{S_k} \approx 0.01 D_{T_k}$

<sup>1</sup> TEOS: MATLAB<sup>®</sup> Oceanographic Toolbox of International Thermodynamic Equation of Seawater-2010 (TEOS-10 standard).

<sup>2</sup> FVCOM: MATLAB<sup>®</sup> Finite Volume Community Ocean Model-toolbox.

(c) Rx Default Parameters

Parameter	Value
Optical filter bandwidth $B_o$	2 nm
LPF bandwidth $B_e$	$\approx R_b/2$
Lens aperture diameter $D_r$	75 mm
SiPM active area $A_{PD}$	9 mm <sup>2</sup>
SiPM, number of SPADs	10998
SiPM, fill factor	48 %
SiPM gain $G$	$10^6$
SiPM photon detection efficiency $\Upsilon_{PDE}$	24 %
SiPM dark count rate $f_{DCR}$	6.6 MHz
SiPM dead-time $\tau_d$	100 ns
SiPM prob. of cross-talk $P_{CT}$	0.03 %
SiPM prob. of after-pulsing $P_{AP}$	0.2 %
SiPM excess noise factor $F$	1.1
TIA load resistance $R_L$	1 k $\Omega$

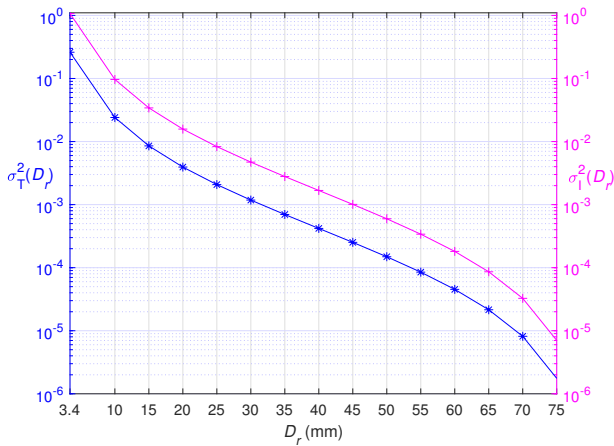
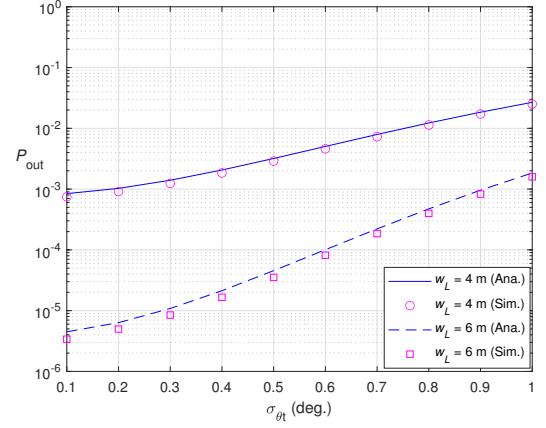
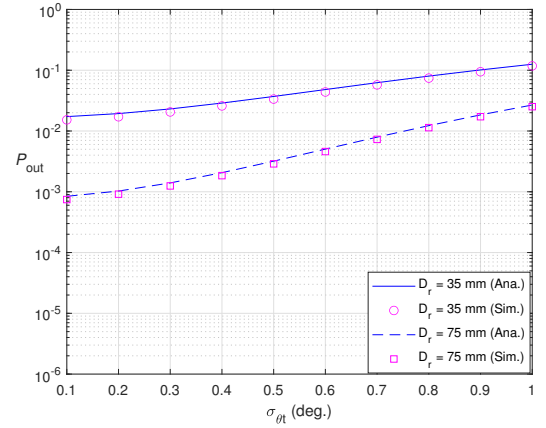


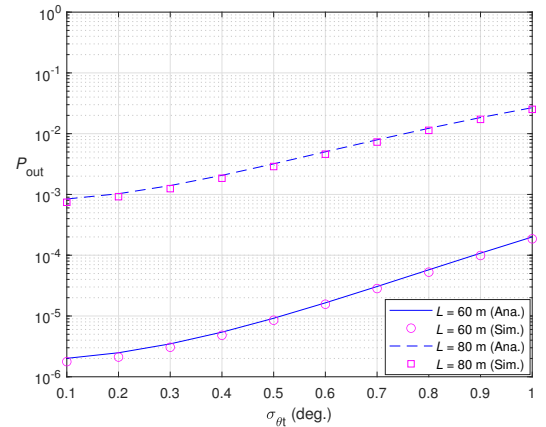
Fig. 5: Impact of the Rx aperture size on  $\sigma_T^2(D_r)$  and the scintillation index  $\sigma_I^2(D_r)$ .  $E_{\text{sun}}(\lambda, 0) = 0$ , perfect beam alignment conditions, i.e.,  $\sigma_{\theta t} = \sigma_{\theta r} = 0$  and  $\sigma_{pt} = \sigma_{pr} = 0$ .



(a)



(b)



(c)

Fig. 6: Effect of PEs on  $P_{\text{out}}$  performance; for  $\theta_{\text{FoVr}} = 4^\circ$ ,  $\sigma_{\theta r} = 0.1^\circ$ ,  $\sigma_{pt} = 1 \text{ m}$  and  $\sigma_{pr} = 1 \text{ m}$ ; (a) effect of beam waist  $w_L$  for  $D_r = 75 \text{ mm}$  and  $L = 80 \text{ m}$ ; (b) effect of aperture diameter for  $w_L = 4 \text{ m}$  and  $L = 80 \text{ m}$ ; (c) effect of link range  $L$  for  $w_L = 4 \text{ m}$  and  $D_r = 75 \text{ mm}$ . “Sim” denotes numerical simulation results and “Ana” refers to analytical upper bounds using (38).

### C. Effect of PEs

First, assuming the absence of solar noise, consider a relatively large Rx FoV where the link interruption can be neglected. As we will show later in Subsection V-D, with the considered link parameters, this corresponds to a  $\theta_{\text{FoVr}}$  of larger than  $\sim 4^\circ$ .

Here, we focus on the Tx angular misalignment parameter  $\sigma_{\theta_t}$ , which is one of the most important PE parameters in practice for the considered scenario. In fact, depending on the buoy size, weight, etc., the severity of sea waves, and whether or not the buoy integrates a stabilization system,  $\sigma_{\theta_t}$  can have different variation ranges. We start by considering a range of less than a few degrees for  $\theta_t$ , which would correspond to the case of a stabilized buoy. Figure 6 presents  $P_{\text{out}}$  plots versus Tx angular misalignment parameter  $\sigma_{\theta_t}$  for other values of beam waist  $w_L$ , Rx aperture diameter  $D_r$ , and link range  $L$ , while the different PE parameters are set to their default values. Both analytical upper bounds (Equation (38)) and simulation-based results are presented (the latter are obtained based on  $10^8$  channel realizations), where we notice that the upper bounds on  $P_{\text{out}}$  are quite tight. Notice that, as shown in the previous subsection, given the relatively large  $D_r$  used, the turbulence effect is negligible, and the link outage is purely due to PEs. Generally, we notice that by increase in the Tx angular misalignment  $\sigma_{\theta_t}$ , the beam spot can be increasingly pointed away from the Rx center (and hence, the PD), resulting in increased  $P_{\text{out}}$ . In Fig. 6(a), the impact of the beam waist  $w_L$  on the link performance is illustrated, where a lower  $P_{\text{out}}$  is reasonably achieved for a larger  $w_L$ . For instance, for  $\sigma_{\theta_t} = 0.5^\circ$ ,  $P_{\text{out}}$  equals  $2.9 \times 10^{-3}$  and  $3.5 \times 10^{-5}$  for  $w_L = 4$  and 6 m, respectively. This is because a larger beam waist casts a wider beam footprint at the Rx plane, hence, its coverage extends closer to the PD center. However, a larger beam waist results in a higher geometric loss at the same time.

Fixing the beam waist to  $w_L = 4$  m, Fig. 6(b) illustrates the effect of the Rx aperture by contrasting  $P_{\text{out}}$  for  $D_r = 35$  and 75 mm. As expected, the link performance is improved for a larger  $D_r$  since there is a larger area to collect most photons that would have been lost due to PEs. Note, in the presence of solar radiation, a larger  $D_r$  also implies a higher level solar noise at the Rx, thus the need to a compromise [7].

Assuming  $w_L = 4$  m and  $D_r = 75$  mm, Fig. 6(c) shows the effect of link range for  $L = 60$  and 80 m. Obviously, a lower  $P_{\text{out}}$  is achieved for a shorter  $L$ , e.g.,  $8.5 \times 10^{-6}$  and  $2.9 \times 10^{-3}$ , respectively, for  $\sigma_{\theta_t} = 0.5^\circ$ . For a shorter range, there is less beam spread, and more photons are captured by the PD. This also suggests that a lower transmit power is required at a shorter distance to achieve a target  $P_{\text{out}}$ .

To further study the impact of transmit power in addition with link range, two case studies are considered in Fig. 7, namely: (a) a tracked system where beam steering is done at the Tx to reduce beam angular misalignment, with  $\sigma_{\theta_t}$  less than  $\sim 1^\circ$ ; (b) and a low-cost system with no beam tracking mechanism nor any buoy stabilization system, with  $\sigma_{\theta_t}$  as large as  $\sim 15^\circ$ . We refer to these cases simply as *tracked* and *non-tracked* systems. To deal with the potentially large

angular misalignment in the later case, a large beam waist of  $w_L = 15$  m is considered, in contrast with  $w_L = 6$  m in the former case.

In order to show the effect of the Tx power at the same time, in addition to the default value of  $P_{\text{Tx},1} = 4$  W, we have considered the case of a relatively low peak Tx power of  $P_{\text{Tx},1} = 0.1$  W. The considered link range  $L$  has been accordingly adjusted depending on  $\sigma_{\theta_t}$  range and  $P_{\text{Tx},1}$  in order to ensure sufficient link reliability. Assuming a target  $P_{\text{out}}$  of  $10^{-3}$ , for instance, we can see from Fig. 7 that with  $P_{\text{Tx},1} = 4$  W, reliable communication can be realized for  $\sigma_{\theta_t}$  less than  $0.9^\circ$  and  $5^\circ$  at  $L = 80$  and 50 m for the cases of tracked and non-tracked systems, respectively. They correspond to less than  $0.8^\circ$  and  $7^\circ$  at  $L = 60$  and 30 m, respectively, with  $P_{\text{Tx},1} = 0.1$  W.

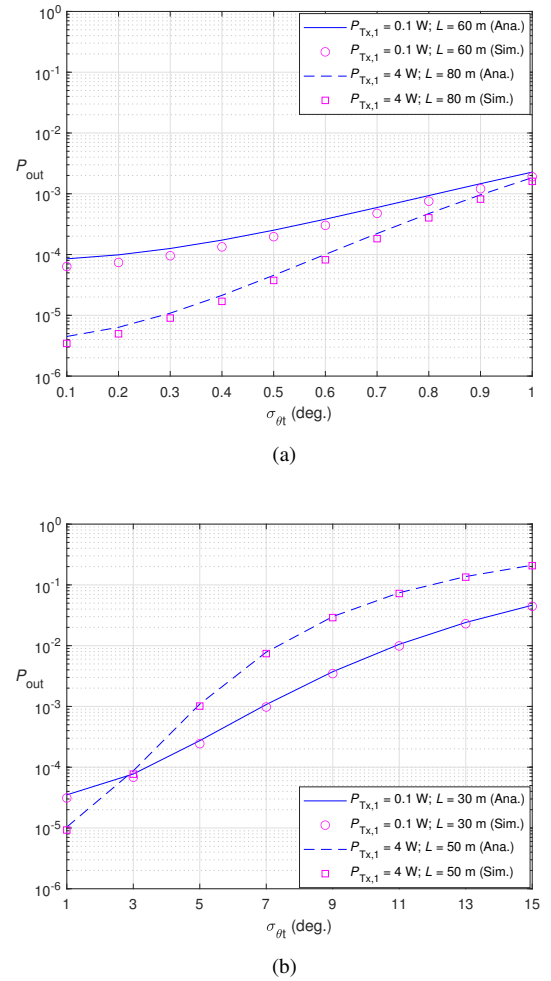


Fig. 7: Outage probability versus Tx angular misalignment parameter  $\sigma_{\theta_t}$  for two cases of  $P_{\text{Tx}} = 0.1$  and 4 W; (a) Tracked system:  $w_L = 6$  m for  $L = 60$  and 80 m;  $\theta_{\text{FoVr}} = 4^\circ$ ,  $\sigma_{\theta_r} = 0.1^\circ$ ,  $\sigma_{pt} = 1$  m and  $\sigma_{pr} = 1$  m; (b) Non-tracked system:  $w_L = 15$  m for  $L = 30$  and 50 m,  $\theta_{\text{FoVr}} = 60^\circ$ ,  $\sigma_{\theta_r} = 1^\circ$ ,  $\sigma_{pt} = 5$  m and  $\sigma_{pr} = 1$  m. “Sim.” and “Ana.” refer to numerical simulation results and analytical upper bounds, respectively.

It is also interesting to note the cross point between the plots at  $\sigma_{\theta_t} \approx 1^\circ$  and  $3^\circ$  in Figs. 7(a) and 7(b), respectively, which

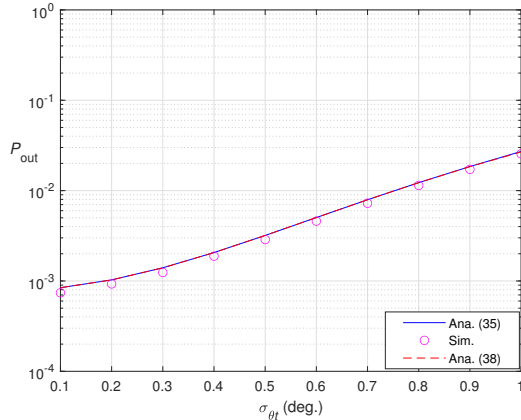
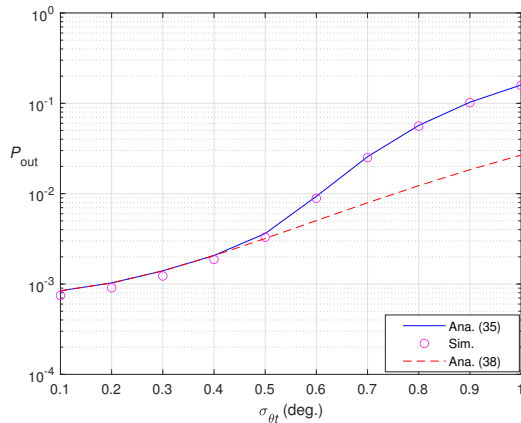
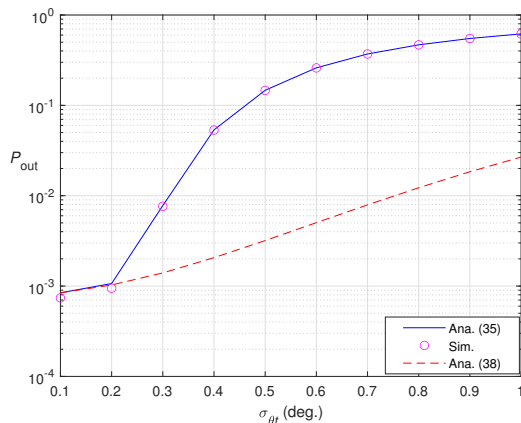
(a)  $\theta_{\text{FoVr}} = 4^\circ$ (b)  $\theta_{\text{FoVr}} = 2^\circ$ (c)  $\theta_{\text{FoVr}} = 1^\circ$ 

Fig. 8: Impact of the limited Rx FoV  $\theta_{\text{FoVr}}$  on the link performance.  $P_{\text{Tx},1} = 4 \text{ W}$ ,  $L = 80 \text{ m}$ ,  $w_L = 4 \text{ m}$ ,  $\sigma_{\theta_r} = 0.1^\circ$ ,  $\sigma_{p_t} = 1 \text{ m}$  and  $\sigma_{p_r} = 1 \text{ m}$ . ‘Sim’ corresponds to simulated results, whereas ‘Ana’ corresponds to analytical upper bounds calculated from (35) and (38) for the cases of limited and unlimited Rx  $\theta_{\text{FoVr}}$ , respectively.

is because of the deteriorated performance due to increased PEs that is more detrimental for a longer link range.

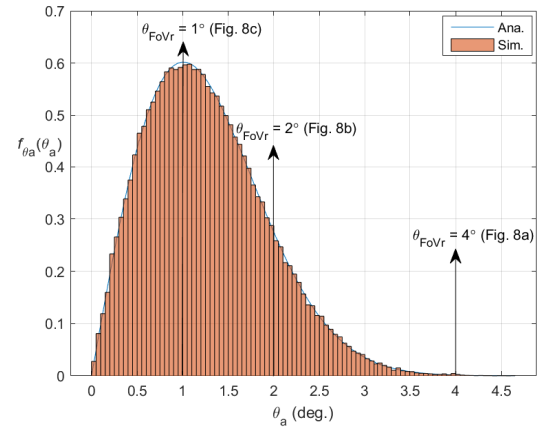


Fig. 9: Distribution of  $\theta_a$  for a tracked system; for  $\sigma_{\theta_t} = 1^\circ$  and  $\sigma_{\theta_r} = 0.1^\circ$ ; ‘Sim’ and ‘Ana’ correspond to simulated and analytical results using (28) and (29).

#### D. Effect of link interruption

Thus far, we have considered the case of a relatively large Rx FoV, where no link interruption occurs since the AoA of the received signal is always less than  $\theta_{\text{FoVr}}$ . In practice, to mitigate the impact of solar radiation, the FoV needs to be limited (see Subsection V-E). Hence, let us now investigate the effect of limited Rx FoV and the link performance degradation due to link interruption due to pointing errors.<sup>8</sup> For this, consider the case of a tracked system (as described in the previous subsection). Figure 8 shows the impact of link interruption across a given range of  $\sigma_{\theta_t}$  for different  $\theta_{\text{FoVr}}$ . Additionally, the histogram of the AoA  $\theta_a$  for the same link parameters is shown in Fig. 9 to better assess the results of Fig. 8.

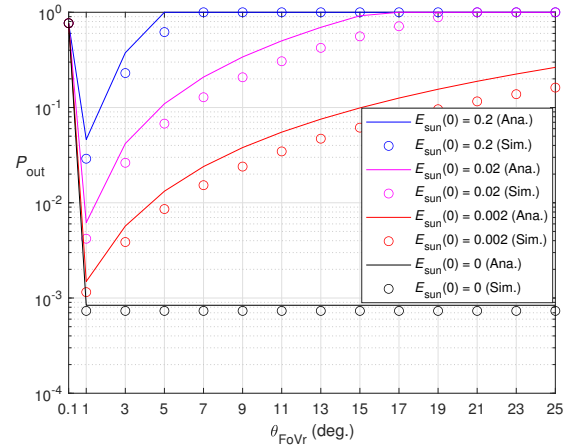
In Fig. 8(a), the considered  $\theta_{\text{FoVr}} = 4^\circ$  is large enough so that the probability of link interruption, i.e.,  $\theta_a > \theta_{\text{FoVr}}$ , is very low, see Fig. 9. For smaller  $\theta_{\text{FoVr}}$  values, as can be seen from Figs. 8(b) and 8(c), the link interruption becomes the major effect impacting  $P_{\text{out}}$ , which can be particularly seen in the latter case. In practice, a larger FoV Rx will collect a larger amount of solar radiation as well, necessitating to make a trade-off between relaxing the impact of link interruption (by using a large FoV) and minimizing performance degradation due to solar noise effect (by setting a small FoV), see the next subsection.

#### E. Effect of solar noise

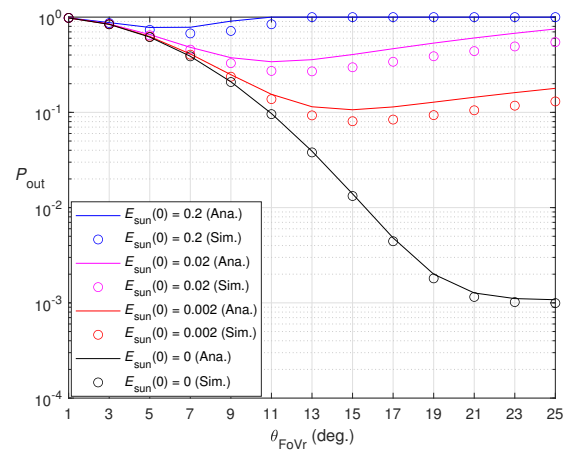
Increasing the Rx FoV improves the link robustness against PEs but it can also affect the link performance in the presence

<sup>8</sup>For the sake of clarity, and in order to compare the results with those of the previous subsection, we assume the absence of solar radiation, and leave the general case to Subsection V-E.

of background noise. To study the impact of solar noise, we have shown in Fig. 10 plots of  $P_{\text{out}}$  with respect to the Rx FoV  $\theta_{\text{FoVr}}$ , for four cases of  $E_{\text{sun}}(\lambda, 0)$  of 0.2, 0.02, 0.002, and  $0 \text{ Wm}^{-2}\text{nm}^{-1}$ . For instance,  $E_{\text{sun}}(\lambda, 0) = 0.2 \text{ Wm}^{-2}\text{nm}^{-1}$  corresponds to  $\lambda = 450 \text{ nm}$  for the sun at  $60^\circ$  with respect to its zenith over a cloudy sky [38]. Two scenarios of tracked and non-tracked beam are considered with the same system parameters as in Fig 7 for both analytical upper bounds and simulation-based results.



(a)



(b)

Fig. 10: Effect of  $\theta_{\text{FoVr}}$  on  $P_{\text{out}}$  for different solar noise levels  $E_{\text{sun}}(\lambda, 0)$  in  $\text{Wm}^{-2}\text{nm}^{-1}$ .  $P_{\text{Tx},1} = 4 \text{ W}$ ,  $D_r = 75 \text{ mm}$ ; (a)  $w_L = 4 \text{ m}$ ,  $L = 80 \text{ m}$ ,  $\sigma_{\theta t} = 0.1^\circ$ ,  $\sigma_{\theta r} = 0.1^\circ$ ,  $\sigma_{pt} = 1 \text{ m}$  and  $\sigma_{pr} = 1 \text{ m}$ ; (b)  $w_L = 15 \text{ m}$ ,  $L = 50 \text{ m}$ ,  $\sigma_{\theta t} = 5^\circ$ ,  $\sigma_{\theta r} = 1^\circ$ ,  $\sigma_{pt} = 5 \text{ m}$  and  $\sigma_{pr} = 1 \text{ m}$ . ‘Ana’ and ‘Sim’ correspond to analytical upper bounds and simulated results, respectively.

As expected, for relatively small  $\theta_{\text{FoVr}}$ ,  $P_{\text{out}}$  improves by increasing the Rx FoV due to reduced PE effect (especially link interruption). However, there is an optimal  $\theta_{\text{FoVr}}$  over which the link performance degrades because of the solar noise effect which becomes dominant. This optimal value depends on the PE parameters (here, tracked or non-tracked scenarios) and the solar noise level at sea surface,  $E_{\text{sun}}(\lambda, 0)$ . Note that for the simple Gaussian lens considered here, changing the FoV does not impact the Rx effective light collection area. Reasonably, in the absence of solar noise (i.e.,  $E_{\text{sun}}(0) = 0$  in Fig. 10),  $P_{\text{out}}$  improves by increasing  $\theta_{\text{FoVr}}$  until a limit beyond which it remains constant due to the fact that it is always larger than the AoA of the incoming beam. Meanwhile, note that the slight difference between the analytical upper bounds and the simulated results is because the analytical expressions were derived assuming negligible background noise at the Rx (see (42), Appendix A).

### F. Optimum parameter selection

In this subsection, we investigate optimal Tx-Rx parameter selection to maximize the performance of a link subject to different channel effects. The considered parameters are the Tx beam divergence angle  $\theta_0$  (which can be adjusted, e.g., by means of a diffuser) and the Rx Fov  $\theta_{\text{FoVr}}$ . For the former, in consistency with the previously presented results, we will consider  $w_L$  instead, although it includes the link range  $L$ . Note that in a previous work [26], the idea of optimum system parameter selection was investigated through a simulation-based approach. Here, however, using (35), the optimum Tx-Rx parameters to achieve the minimum  $P_{\text{out}}$  are analytically calculated. This is done by calculating the minimum of  $P_{\text{out}}$  in (35) as a function of the two variables  $w_L$  and  $\theta_{\text{FoVr}}$ . In this work, as alternative to solving (35) by differentiation, we have used the *fmincon* function of MATLAB<sup>®</sup> to compute the optimum parameters.

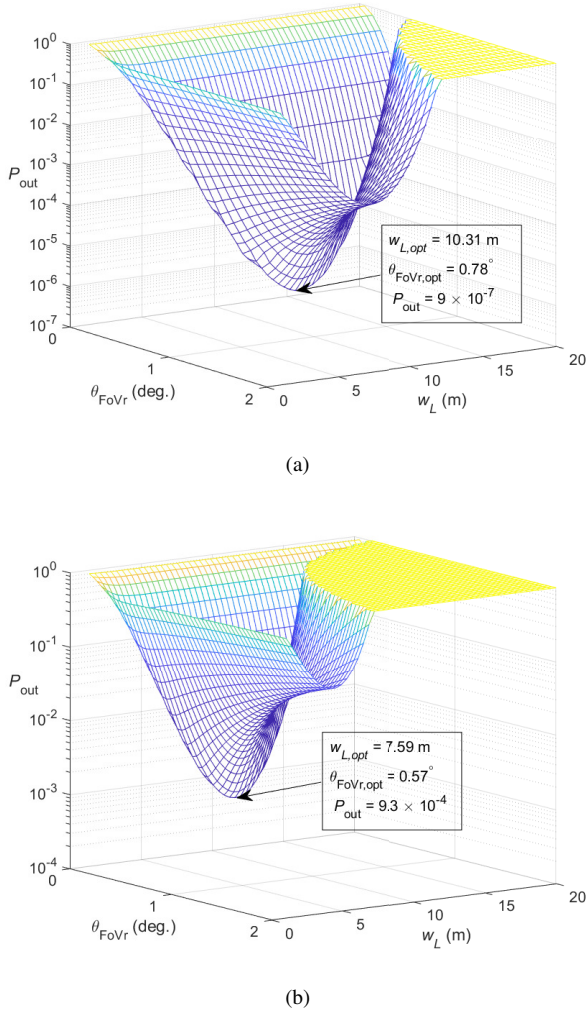


Fig. 11: Link parameter optimization for (a)  $E_{\text{sun}}(\lambda, 0) = 0.02$  and (b)  $E_{\text{sun}}(\lambda, 0) = 0.2 \text{ Wm}^{-2} \text{ nm}^{-1}$ . PE and other link parameters correspond to Fig. 10(a).

Figure 11 shows the 3D plot of  $P_{\text{out}}$  (using simulations) with varying  $w_L$  and  $\theta_{\text{FoVr}}$  for the two cases of  $E_{\text{sun}}(\lambda, 0) = 0.02$  and  $0.2 \text{ Wm}^{-2} \text{ nm}^{-1}$ . At the optimum parameters, denoted by  $w_{L,\text{opt}}$  and  $\theta_{\text{FoVr,opt}}$ , the minimum of  $P_{\text{out}}$  is achieved, which is about  $9 \times 10^{-7}$  and  $9.3 \times 10^{-4}$ , for the above-mentioned  $E_{\text{sun}}(\lambda, 0)$ , respectively. Notice the significant improvement that can be achieved in the link performance by using the optimum values of  $w_L$  and  $\theta_{\text{FoVr}}$ . Reasonably, as the intensity of the solar radiation increases, the optimum Rx FoV  $\theta_{\text{FoVr,opt}}$  decreases to reduce the amount of solar radiation captured at the Rx. The relatively small value of  $\theta_{\text{FoVr,opt}}$  is due to the relatively high solar noise level and small beam misalignment, considered here. There is a lower dependency of  $P_{\text{out}}$  to  $\theta_{\text{FoVr}}$  for the lower solar noise level case (although it is mildly distinguishable in the presented figures), which is because less background noise is captured at the Rx. In the absence of background noise, there is not a unique  $\theta_{\text{FoVr,opt}}$ ; in fact, in that case,  $\theta_{\text{FoVr}}$  should just be large enough to minimize the PE effect (as it was also noticed in Fig. 10).

To see the impact of optimal parameter selection on the link performance under different link conditions, Table II shows the optimum  $w_L$  and  $\theta_{\text{FoVr}}$  and the corresponding  $P_{\text{out}}$  for different values of  $\sigma_{\theta t}$  and link range  $L$ . In addition to the analytical results (as described at the beginning of this subsection), we have also presented simulation-based results, where we notice the consistency in the trend of the optimum parameters. Note that the difference between the analytical and simulation results is because the former assumes negligible background noise compared to the signal-dependent shot noise.

From Table II(a), with increased  $\sigma_{\theta t}$ , the optimum beam width  $w_{L,\text{opt}}$  reduces to make the beam more directive, hence reducing the geometric loss and the probability that a large portion of the beam footprint at the Rx plane falls outside the Rx aperture. Meanwhile, the resulting increased risk of beam misalignment is compensated with increased optimum Rx FoV  $\theta_{\text{FoVr,opt}}$ . On the other hand, from Table II(b), with increased  $L$ , the optimum beam width  $w_{L,\text{opt}}$  is decreased to allow a narrower beam, hence incurring less geometric loss at a longer range. Meanwhile,  $\theta_{\text{FoVr,opt}}$  changes mildly since it mainly depends on  $\sigma_{\theta t}$ , which is kept constant for Table II(b) results.

## VI. CONCLUSIONS AND DISCUSSIONS

We considered a vertical UWOC link subject to PEs, oceanic turbulence, and solar noise, and investigated the outage probability performance of the link under different realistic operational conditions. Analytical upper bound expressions were derived for the link outage probability, which were shown to be very tight, in particular, for low background noise levels. We demonstrated the effect of different link and PE parameters on the performance. Also, we elucidated the impact of oceanic turbulence, where, in particular, it was shown that the turbulence effect is practically negligible when using a lens at the Rx, even of relatively small size due to the aperture averaging effect. Concerning PEs, we showed the trade-off between the Tx beam width and the link range, or otherwise the Tx power in achieving a required link reliability. The interest of optimum parameter selection for the Tx/Rx was further investigated, which was shown to allow significant performance improvement by making compromise, especially, regarding the effects of PEs and solar radiation. It is worth mentioning that for increased water turbidity and, consequently, beam spreading, there will be less sensitivity to beam misalignment, compared to the clear ocean water case, considered in this paper [4].

Throughout the paper, we focused on the downlink in the considered vertical beam scenario. The extension of this study to the case of uplink transmission, i.e., from the AUV to the buoy is subject of future research, which is, nevertheless, less problematic. As a matter of fact, our choice of focusing on the downlink is justified by the fact that the surface platform is much more subject to inclinations and displacements, compared to the underwater platform, therefore the link performance is more considerably subject to PEs.

TABLE II: Optimum  $w_L$  and  $\theta_{\text{FoVr}}$  values and the corresponding  $P_{\text{out}}$  for: (a) Fixed  $L = 80$  m and changing  $\sigma_{\theta_t}$ ; (b) Fixed  $\sigma_{\theta_t} = 0.1^\circ$  and changing  $L$ .  $P_{\text{Tx},1} = 4$  W,  $E_{\text{sun}}(\lambda, 0) = 0.2 \text{ Wm}^{-2} \text{ nm}^{-1}$ ,  $\sigma_{\theta_r} = 0.1^\circ$ ,  $\sigma_{p_t} = \sigma_{p_r} = 1$  m.

(a)						
$\sigma_{\theta_t}$ (deg.)	Simulation based			Analytical upper bounds		
	$w_{L,\text{opt}}$ (m)	$\theta_{\text{FoVr,opt}}$ (deg.)	$P_{\text{out}}$	$w_{L,\text{opt}}$ (m)	$\theta_{\text{FoVr,opt}}$ (deg.)	$P_{\text{out}}$
0.1	7.59	0.57	$9.3 \times 10^{-4}$	7.09	0.52	$2.7 \times 10^{-3}$
0.5	5.27	1.36	$9.69 \times 10^{-2}$	4.67	1.29	$1.4 \times 10^{-1}$
1	4.1	2.17	$4.06 \times 10^{-1}$	3.75	2.05	$4.88 \times 10^{-1}$

(b)						
$L$ (m)	Simulation based			Analytical upper bounds		
	$w_{L,\text{opt}}$ (m)	$\theta_{\text{FoVr,opt}}$ (deg.)	$P_{\text{out}}$	$w_{L,\text{opt}}$ (m)	$\theta_{\text{FoVr,opt}}$ (deg.)	$P_{\text{out}}$
80	7.59	0.57	$9.3 \times 10^{-4}$	7.09	0.52	$2.7 \times 10^{-3}$
90	4.49	0.45	$7.8 \times 10^{-2}$	4.47	0.38	$1.05 \times 10^{-1}$
100	2.55	0.35	$4.43 \times 10^{-1}$	2.53	0.33	$4.9 \times 10^{-1}$

Also, the impact of solar radiation will be less important for uplink transmission.

#### ACKNOWLEDGMENT

This work was partly supported by Alex Ekwueme Federal University Ndufu-Alike (AE-FUNAI) in partnership with the Embassy of France in Nigeria and Campus France. This publication is also based upon work from COST Action CA19111 (European Network on Future Generation Optical Wireless Communication Technologies, NEWFOCUS), supported by COST (European Cooperation in Science and Technology). The authors would also like to thank Prof. Hassan Akhouayri from Fresnel Institute, Marseille, Mr. Yves Chardard from SubseaTech Co., Marseille, and Mr. Christian Marfia from IFREMER, La Seyne-sur-Mer, France, for the fruitful discussions regarding the optoelectronic components as well as the practical parameters for AUV/buoy transmission scenarios, as well as Prof. Bruno Fracasso from IMT-Atlantique, Brest, France, for the consideration of practical tracked and no-tracked transmission system parameters.

#### APPENDIX

Given the assumption of using a high-gain SiPM, we reasonably assume that the shot noise is the dominant noise source at the Rx. It was verified that, even if a relatively large OOK extinction ratio  $\xi$  is used, even for ‘‘off’’ OOK symbols, the thermal, dark and solar noises are negligible, compared with the signal-dependent shot noise. As a result, given that  $P_{\text{Tx},0} = \xi P_{\text{Tx},1}$ , we consider  $\check{r}_0 \approx \xi \check{r}_1$  and  $\sigma_{n_0}^2 \approx \xi \sigma_{n_1}^2$ . Hence, the optimal OOK detection threshold in (9) is simplified as

$$\gamma_{\text{th}} \approx R_L \sqrt{\xi I_{s,1}^2 - \frac{\xi \sigma_{n_1}^2}{1 - \xi} \log \xi} \approx R_L I_{s,1} \sqrt{\xi} \approx R_L I_{s,0} \sqrt{\frac{1}{\xi}} \quad (39)$$

Using this, (8) can be approximated as

$$P_e(e|h) \approx \frac{1}{2} \text{erfc} \left( \frac{R_L I_{s,0} \left( \sqrt{\frac{1}{\xi}} - 1 \right)}{\sqrt{2 \sigma_{n_0}^2}} \right). \quad (40)$$

Using the notations  $\alpha = 2eGF B_e R_L \omega$ ,  $\omega = R_L \mathcal{R}_e P_{\text{Tx},0}$ , and  $\beta = R_L^2 \sigma_d^2 + R_L^2 \sigma_b^2 + \sigma_{\text{th}}^2$ , (40) can be re-written as

$$P_e(e|h) = \frac{1}{2} \text{erfc} \left( \frac{\omega h \left( \sqrt{\frac{1}{\xi}} - 1 \right)}{\sqrt{2 \alpha h + 2 \beta}} \right). \quad (41)$$

The channel threshold  $h_{\text{th}}$ , such that  $P_e(e|h_{\text{th}}) = \text{BER}_{\text{th}}$ , can be obtained from (41) as

$$h_{\text{th}} = \frac{\mathcal{B} + \sqrt{\mathcal{B}^2 + 4 \mathcal{A} \mathcal{C}}}{2 \mathcal{A}}, \quad (42)$$

where  $\mathcal{A} = \left( \omega \sqrt{\frac{1}{\xi}} - \omega \right)^2$ ,  $\mathcal{B} = \alpha \mathcal{D}^2$ ,  $\mathcal{C} = \beta \mathcal{D}^2$ ,  $\mathcal{D} = Q^{-1}(\text{BER}_{\text{th}})$ , and  $Q^{-1}$  is the inverse Q-function.

Considering a circular lens of diameter  $D_r$ , the scintillation index corresponding to the  $k^{\text{th}}$  layer, denoted by  $\sigma_{I_k}^2(D_r)$ , is given in (43) [42] where  $\kappa$  is the magnitude of the spatial frequency,  $\Phi_{n_k}(\kappa)$  is the spatial power spectrum model of oceanic turbulence for the  $k^{\text{th}}$  layer,  $\Omega_{G_k} = 16L_k/\mathcal{K}D_r^2$  is a dimensionless parameter characterizing the spot radius of the Rx lens,  $\Lambda_{0_k} = L_k/\mathcal{K}\alpha_s^2$ ,  $\Lambda_{1_k} = \Lambda_{0_k}/(\Theta_{0_k}^2 + \Lambda_{0_k}^2)$ , where  $\Theta_{0_k} = 1 - L_k/F_0$ , with  $F_0$  the beam radius of curvature. Also in (43),  $\Theta_{1_k} = 1 - \Theta_{1_k}$  with  $\Theta_{1_k} = \Theta_{0_k}/(\Theta_{0_k}^2 + \Lambda_{0_k}^2)$ , and  $\Phi_{n_k}(\kappa)$  denotes the corresponding  $k^{\text{th}}$ -layer turbulence power spectrum, which is given by (45) [54]. where  $\epsilon$  is the dissipation rate of kinetic energy per unit mass of fluid,  $\mathcal{X}_T$  is the dissipation rate of mean-squared temperature, and the constants  $C_0$  and  $C_1$  are equal to 0.72 and 2.35 [54], respectively. Further defined are the parameters specific to the  $k^{\text{th}}$  layer: The Prandtl numbers for temperature and salinity are given by  $P_{T_k} = \nu_k D_{T_k}^{-1}$  and  $P_{S_k} = \nu_k D_{S_k}^{-1}$ , respectively, where  $\nu_k$  is the kinematic viscosity, and  $D_{T_k}$  and  $D_{S_k}$  are molecular diffusivity of temperature and salinity, respectively. The term  $P_{TS_k}$  is one-half of the harmonic mean of  $P_{T_k}$  and  $P_{S_k}$ . Also,  $\delta_k = 1.5C_1^2(\kappa\eta_k)^{2/3} + C_1^3(\kappa\eta_k)^2$ , where  $\eta_k = (\nu_k^3/\epsilon)^{1/4}$  is the Kolmogorov micro-scale length. Furthermore,  $\omega_k$  in (45) denotes the relative strength of temperature and salinity fluctuations. Considering  $(dT_0/dz)_k$  and  $(dS_0/dz)_k$  as the temperature and salinity differences between top and bottom boundaries of the  $k^{\text{th}}$  layer, respectively, then [55, 56, 57]

$$\sigma_{I_k}^2(D_r) = 8\pi^2 \mathcal{K}^2 L_{T_k} \int_0^1 \int_0^\infty \kappa \Phi_{n_k}(\kappa) \exp \left\{ -\frac{L_{T_k} \kappa^2 \left[ (1 - \bar{\Theta}_{1_k} \xi)^2 + \wedge_{1_k} \Omega_{G_k} \xi^2 \right]}{\mathcal{K} (\Omega_{G_k} + \wedge_{1_k})} \right\} \quad (43)$$

$$\times \left\{ 1 - \cos \left[ \frac{L_{T_k} \kappa^2 (\Omega_{G_k} - \wedge_{1_k})}{\mathcal{K} (\Omega_{G_k} + \wedge_{1_k})} \xi (1 - \bar{\Theta}_{1_k} \xi) \right] \right\} d\kappa d\xi, \quad (44)$$

$$\Phi_{n_k}(\kappa) = (4\pi\kappa^2)^{-1} C_0 \left( \frac{\alpha_k^2 \mathcal{X}_T}{\omega_k^2} \right) \epsilon^{-1/3} \kappa^{-5/3} \left( 1 + C_1 (\kappa \eta_k)^{2/3} \right) \left[ \omega_k^2 \exp(-C_0 C_1^{-2} P_{T_k}^{-1} \delta_k) + d_{r_k} \exp(-C_0 C_1^{-2} P_{S_k}^{-1} \delta_k) - \omega_k (d_{r_k} + 1) \exp(-0.5 C_0 C_1^{-2} P_{TS_k}^{-1} \delta_k) \right] \quad (45)$$

$$\omega_k = \frac{\alpha_k (dT0/dz)_k}{\beta_k (dS0/dz)_k}, \quad (46)$$

where  $\alpha_k$  is the thermal expansion coefficient and  $\beta_k$  is the saline contraction coefficient. Lastly, the eddy diffusivity ratio  $d_{r_k}$  in (45) is given by [55, 56, 57]

$$d_{r_k} \approx \begin{cases} |\omega_k| \left( |\omega_k| - \sqrt{|\omega_k| (|\omega_k| - 1)} \right)^{-1}, & |\omega_k| \geq 1 \\ 1.85|\omega_k| - 0.85, & 0.5 \leq |\omega_k| \leq 1 \\ 0.15|\omega_k|. & |\omega_k| < 0.5 \end{cases} \quad (47)$$

In this paper, for the calculation of the scintillation index, we assume  $F_0 = \infty$ , which corresponds to a collimated beam.

Here, we explain our approach for deriving the closed form asymptotic expression of Equation (35). Using (34), (13), (26), (15), and the definition of  $P_{\text{out}}$  in (11), after some mathematical developments,  $P_{\text{out}}$  can be written as in (50). Considering variable change of  $X = (\ln(h_t) - \mu_T) / \sqrt{2\sigma_T^2}$  and using [58, Section 2.33, Eq.(1)] then (50) can be rewritten as in (51), where  $X_l = (\ln(h) - \ln(A_0 h_c) - \mu_T) / \sqrt{2\sigma_T^2}$ . Now, defining  $Y$  as

$$Y = \sqrt{2\sigma_T^2} \frac{w_{Leq}^2}{8\sigma_{r_d}^2} + \frac{(-\ln(A_0 h_c) - \mu_T)}{\sqrt{2\sigma_T^2}} + \ln(h) \frac{1}{\sqrt{2\sigma_T^2}}, \quad (48)$$

then, (51) can be expressed as in (52), where

$$Y_u = \sqrt{2\sigma_T^2} \frac{w_{Leq}^2}{8\sigma_{r_d}^2} + \frac{(-\ln(A_0 h_c) - \mu_T)}{\sqrt{2\sigma_T^2}} + \ln(h_{\text{th}}) \frac{1}{\sqrt{2\sigma_T^2}}. \quad (49)$$

The integration in (52) can be solved by using [59, Section 4.2, Eq.(2)] and further simplified as in (53).

Lastly, for  $h_{\text{th}} \rightarrow 0$ , (53) can be simplified as in (35).

## REFERENCES

- [1] M. A. Khalighi, C. J. Gabriel, L. M. Pessoa, and B. Silva, *Visible Light Communications: Theory and Applications*. CRC-Press, 2017, ch. Underwater Visible Light Communications, Channel Modeling and System Design, pp. 337–372.
- [2] M. A. Khalighi, C. Gabriel, T. Hamza, S. Bourennane, P. Léon, and V. Rigaud, “Underwater wireless optical communication; recent advances and remaining challenges,” *IEEE International Conference on Transparent Optical Networks (ICTON)*, pp. 1–4, July 2014, invited paper, Graz, Austria.
- [3] X. Sun, C. H. Kang, M. Kong, O. Alkhazragi, Y. Guo, M. Ouhssain, Y. Weng, B. H. Jones, T. K. Ng, and B. S. Ooi, “A review on practical considerations and solutions in underwater wireless optical communication,” *J. Lightw. Technol.*, vol. 38, no. 2, pp. 421–431, Jan. 2020.
- [4] B. Cochenour, L. Mullen, and J. Muth, “Temporal response of the underwater optical channel for high-bandwidth wireless laser communications,” *IEEE J. Ocean. Eng.*, vol. 38, no. 4, pp. 730–742, Oct. 2013.
- [5] M. Doniec, M. Angermann, and D. Rus, “An end-to-end signal strength model for underwater optical communications,” *IEEE J. Ocean. Eng.*, vol. 38, no. 4, pp. 743–757, Oct. 2013.
- [6] C. Gabriel, M. A. Khalighi, S. Bourennane, P. Léon, and V. Rigaud, “Monte-carlo-based channel characterization for underwater optical communication systems,” *IEEE/OSA J. Opt. Commun. Netw.*, vol. 5, no. 1, pp. 1–12, Jan. 2013.
- [7] T. Hamza, M. A. Khalighi, S. Bourennane, P. Léon, and J. Opderbecke, “Investigation of solar noise impact on the performance of underwater wireless optical communication links,” *Optics Express*, vol. 24, no. 22, pp. 25 832–25 845, Oct. 2016.
- [8] J. W. Giles and I. N. Bankman, “Underwater optical communication systems. part 2 : Basic design considerations,” *Military Communications Conference (MILCOM)*, vol. 3, pp. 1700–1705, Oct. 2005, Atlantic City, NJ, USA.
- [9] O. Korotkova, N. Farwell, and E. Shchepakina, “Light scintillation in oceanic turbulence,” *Waves in Random and Complex Media*, vol. 22, no. 2, pp. 260–266, 2012.
- [10] C. Gabriel, M. A. Khalighi, S. Bourennane, P. Léon, and V. Rigaud, “Misalignment considerations on point-to-point underwater wireless optical links,” *IEEE OCEANS Conference*, June 2013, Bergen, Norway.
- [11] S. Tang, Y. Dong, and X. Zhang, “On link misalignment for underwater wireless optical communications,” *IEEE Commun. Lett.*, vol. 16, no. 10, pp. 1688–1690, 2012.
- [12] A. S. Ghazy, S. Hranilovic, and M. A. Khalighi, “Angular MIMO for underwater wireless optical communications: Link modelling and tracking,” *IEEE J. Ocean. Eng.*, vol. 46, no. 4, pp. 1391–1407, 2021.
- [13] M. A. Khalighi, T. Hamza, S. Bourennane, P. Léon, and J. Opderbecke, “Underwater wireless optical communications using silicon photo-multipliers,” *IEEE Photon. J.*, vol. 9, no. 4, 2017.
- [14] G. Nootz, E. Jarosz, F. R. Dalgleish, and W. Hou, “Quantification of optical turbulence in the ocean and its effects on beam propagation,” *Applied Optics*, vol. 55, no. 31, pp. 8813–8820, 2016.

$$P_{\text{out}} = \frac{(A_0 h_c)^{-\frac{w_{Leq}^2}{4\sigma_{rd}^2}}}{\sqrt{\pi}} \frac{w_{Leq}^2}{4\sigma_{rd}^2} \int_0^{h_{\text{th}}} h^{\frac{w_{Leq}^2}{4\sigma_{rd}^2}-1} F_{\theta_a}(\theta_{\text{FoVr}}) dh \int_{\frac{h}{A_0 h_c}}^{\infty} h_t^{-\frac{w_{Leq}^2}{4\sigma_{rd}^2}-1} \frac{1}{\sqrt{2\sigma_T^2}} \exp\left(-\frac{(\ln(h_t) - \mu_T)^2}{2\sigma_T^2}\right) dh_t$$

$$+ \int_0^{h_{\text{th}}} (1 - F_{\theta_a}(\theta_{\text{FoVr}})) \delta(h)$$
(50)

$$P_{\text{out}} = \left[ (A_0 h_c)^{-\frac{w_{Leq}^2}{4\sigma_{rd}^2}} \frac{w_{Leq}^2}{8\sigma_{rd}^2} \exp\left(-\mu_T \frac{w_{Leq}^2}{4\sigma_{rd}^2}\right) \exp\left(\sigma_T^2 \frac{w_{Leq}^4}{32\sigma_{rd}^4}\right) \int_0^{h_{\text{th}}} h^{\frac{w_{Leq}^2}{4\sigma_{rd}^2}-1} \text{erfc}\left(\sqrt{2\sigma_T^2} \frac{w_{Leq}^2}{8\sigma_{rd}^2} + X_l\right) dh \right] F_{\theta_a}(\theta_{\text{FoVr}})$$

$$+ (1 - F_{\theta_a}(\theta_{\text{FoVr}}))$$
(51)

$$P_{\text{out}} = \frac{(A_0 h_c)^{-\frac{w_{Leq}^2}{4\sigma_{rd}^2}}}{\sqrt{2\sigma_T^2}} \frac{w_{Leq}^2}{8\sigma_{rd}^2} \exp\left(-\mu_T \frac{w_{Leq}^2}{4\sigma_{rd}^2}\right) \exp\left(\sigma_T^2 \frac{w_{Leq}^4}{32\sigma_{rd}^4}\right) \exp\left(-\left(\frac{w_{Leq}^2}{8\sigma_{rd}^2} + \frac{(-\ln(A_0 h_c) - \mu_T)}{2\sigma_T^2}\right) \frac{w_{Leq}^2}{4\sigma_{rd}^2}\right)$$

$$\times \left[ \int_{-\infty}^{Y_u} \exp\left(\frac{Y}{\sqrt{2\sigma_T^2}} \frac{w_{Leq}^2}{4\sigma_{rd}^2}\right) \text{erfc}(Y) dY \right] F_{\theta_a}(\theta_{\text{FoVr}}) + (1 - F_{\theta_a}(\theta_{\text{FoVr}}))$$
(52)

$$P_{\text{out}} = \frac{(A_0 h_c)^{-\frac{w_{Leq}^2}{4\sigma_{rd}^2}}}{2} \exp\left(-\mu_T \frac{w_{Leq}^2}{4\sigma_{rd}^2}\right) \exp\left(\sigma_T^2 \frac{w_{Leq}^4}{32\sigma_{rd}^4}\right) \left[ h_{\text{th}}^{\frac{w_{Leq}^2}{4\sigma_{rd}^2}} \text{erfc}\left(\frac{2\sigma_T^2 w_{Leq}^2 + 8\sigma_{rd}^2 (\ln(h_{\text{th}}) - \ln(A_0 h_c) - \mu_T)}{8\sigma_{rd}^2 \sqrt{2\sigma_T^2}}}\right)\right.$$

$$\left. + \exp\left(\frac{1}{\sigma_T^2} \frac{w_{Leq}^4}{128\sigma_{rd}^4}\right) \exp\left(-\frac{8\sigma_{rd}^2 \sigma_T^2 w_{Leq}^4 - 32\sigma_{rd}^4 w_{Leq}^2 (-\ln(A_0 h_c) - \mu_T)}{256\sigma_{rd}^6 \sigma_T^2}\right) \right]$$

$$\times \text{erfc}\left(\frac{-2\sigma_T^2 w_{Leq}^2 - 8\sigma_{rd}^2 (\ln(h_{\text{th}}) - \ln(A_0 h_c) - \mu_T) + w_{Leq}^2}{8\sigma_{rd}^2 \sqrt{2\sigma_T^2}}}\right) F_{\theta_a}(\theta_{\text{FoVr}}) + (1 - F_{\theta_a}(\theta_{\text{FoVr}})).$$
(53)

- 
- [15] Y. Baykal, "Signal-to-noise ratio reduction due to oceanic turbulence in oceanic wireless optical communication links," *Optics Commun.*, vol. 427, pp. 44–47, 2018.
- [16] E. Zedini, H. M. Oubei, A. Kammoun, M. Hamdi, B. S. Ooi, and M.-S. Alouini, "Unified statistical channel model for turbulence-induced fading in underwater wireless optical communication systems," *IEEE Trans. Commun.*, vol. 67, no. 4, pp. 2893–2907, Apr. 2019.
- [17] M. Elamassie and M. Uysal, "Vertical underwater visible light communication links: Channel modeling and performance analysis," *IEEE Trans. Commun.*, vol. 19, no. 10, pp. 6948–6959, 2020.
- [18] G. Kullenberg, *Pollutant Transfer and Transport in the Sea: Volume II*. CRC-Press, 2018.
- [19] M. C. Gökçe and Y. Baykal, "Aperture averaging and BER for Gaussian beam in underwater oceanic turbulence," *Optics Commun.*, vol. 410, pp. 830–835, 2018.
- [20] I. Toselli and S. Gladysz, "Improving system performance by using adaptive optics and aperture averaging for laser communications in oceanic turbulence," *Optics Express*, vol. 28, no. 12, pp. 17 347–17 361, 2020.
- [21] Y. Fu, C. Huang, and Y. Du, "Effect of aperture averaging on mean bit error rate for UWOC system over moderate to strong oceanic turbulence," *Optics Commun.*, vol. 451, pp. 6–12, 2019.
- [22] R. A. Khalil, M. I. Babar, N. Saeed, T. Jan, and H.-S. Cho, "Effect of link misalignment in the optical-internet of underwater things," *MDPI Electron.*, vol. 9, no. 4, p. 646, Apr. 2020.
- [23] Y. Dong, S. Tang, and X. Zhang, "Effect of random sea surface on downlink underwater wireless optical communications," *IEEE Commun. Lett.*, vol. 17, no. 11, pp. 2164–2167, Nov. 2013.
- [24] H. Zhang, Y. Dong, and L. Hui, "On capacity of downlink underwater wireless optical MIMO systems with random sea surface," *IEEE Commun. Lett.*, vol. 19, no. 12, pp. 2166–2169, Dec 2015.
- [25] A. S. Ghazy, S. Hranilovic, and M. A. Khalighi, "Angular MIMO for underwater wireless optical communications: Channel modelling and capacity," in *2019 16th Canadian Workshop on Information Theory (CWIT)*, June 2019, pp. 1–6, Hamilton, ON, Canada.
- [26] I. C. Ijeh, M. A. Khalighi, and S. Hranilovic, "Parameter optimization for an underwater optical wireless vertical link subject to link misalignments," *IEEE J. Ocean. Eng.*, vol. 46, no. 4, pp. 1424–1437, 2021.
- [27] GROW Project, <https://grow.inesctec.pt>, [Accessed: January 13, 2023].
- [28] F. B. Teixeira, N. Moreira, R. Campos, and M. Ricardo, "Data muling approach for long-range broadband underwater communications," in *International Conference on Wireless and Mobile Computing, Networking and Communications (WiMob)*, 2019, pp. 1–4, Barcelona, Spain.
- [29] S. Li, L. Yang, D. B. da Costa, J. Zhang, and M.-S. Alouini, "Performance analysis of mixed RF-UWOC dual-hop transmission systems," *IEEE Trans. Veh. Technol.*, vol. 69, no. 11, pp. 14 043–14 048, 2020.
- [30] M. A. Khalighi, H. Akhoughyari, and S. Hranilovic, "Silicon-photon-multiplier-based underwater wireless optical communication using pulse-amplitude modulation," *IEEE J. Ocean. Eng.*, vol. 45, no. 4, pp. 1611–1621, 2020.



- [31] *Introduction to SiPM, Technical Note.* ON Semiconductor® - SensL, 2011 (Rev. 6.0, Feb. 2017), available at <https://www.sensl.com/downloads/ds/TN%20-%20Intro%20to%20SPM%20Tech.pdf>.
- [32] L. C. Andrews and R. L. Phillips, *Laser Beam Propagation through Random Media*, 2005.
- [33] T. Essalih, M. A. Khalighi, S. Hranilovic, and H. Akhouayri, "Optical ofdm for SiPM-based underwater optical wireless communication links," *Sensors*, vol. 20, no. 21, p. 6057, 2020.
- [34] C. Mobley, *Light and Water: Radiative Transfer in Natural Waters*. Academic Press, 1994.
- [35] T. Hamza, "Underwater wireless optical communications: Long-range high-data-rate transmission and performance analysis," Ph.D. dissertation, École Centrale Marseille, Mar. 2017.
- [36] F. Xu, M. A. Khalighi, and S. Bourennane, "Impact of different noise sources on the performance of PIN- and APD-based FSO receivers," *COST IC0802 Workshop, IEEE ConTEL Conference*, pp. 211–218, June 2011, Graz, Austria.
- [37] M. T. Dabiri, S. M. S. Sadough, and M. A. Khalighi, "FSO channel estimation for OOK modulation with APD receiver over atmospheric turbulence and pointing errors," *Optics Commun.*, vol. 402, pp. 577–584, 2017.
- [38] C. Mobley, E. Boss, and C. Roesler, *Ocean Optics Web Book*, <http://www.oceanopticsbook.info/>, last accessed: 16 Dec. 2021.
- [39] H. Kaushal and G. Kaddoum, "Underwater optical wireless communication," *IEEE Access*, vol. 4, pp. 1518–1547, Apr. 2016.
- [40] Global Ocean Data Assimilation Experiment (GODAE), <https://nrlgodae1.nrlmry.navy.mil/index.html>, [Accessed: January 13, 2023].
- [41] M. V. Jamali, A. Mirani, A. Parsay, B. Abolhassani, P. Nabavi, A. Chizari, P. Khorramshahi, S. Abdollahramezani, and J. A. Salehi, "Statistical studies of fading in underwater wireless optical channels in the presence of air bubble, temperature, and salinity random variations," *IEEE Trans. Commun.*, vol. 66, no. 10, pp. 4706–4723, 2018.
- [42] L. C. Andrews, R. L. Phillips, and C. Y. Hopen, *Laser Beam Scintillation with Applications*. SPIE press, 2001, vol. 99.
- [43] M.-A. Khalighi, N. Schwartz, N. Aitamer, and S. Bourennane, "Fading reduction by aperture averaging and spatial diversity in optical wireless systems," *IEEE/OSA J. Opt. Commun. Netw.*, vol. 1, no. 6, pp. 580–593, 2009.
- [44] R. Boluda-Ruiz, A. García-Zambrana, B. Castillo-Vázquez, and S. Hranilovic, "Impact of angular pointing error on BER performance of underwater optical wireless links," *Optics Express*, vol. 28, no. 23, pp. 34 606–34 622, Nov 2020.
- [45] B. E. A. Saleh and M. C. Teich, *Fundamentals of Photonics*. New York: Wiley, 1991.
- [46] M. T. Dabiri, S. M. S. Sadough, and M. A. Khalighi, "Channel modeling and parameter optimization for hovering UAV-based free-space optical links," *IEEE J. Sel. Areas Commun.*, vol. 36, no. 9, pp. 2104–2113, Sep. 2018.
- [47] A. A. Farid and S. Hranilovic, "Outage capacity optimization for free-space optical links with pointing errors," *J. Lightw. Technol.*, vol. 25, no. 7, pp. 1702–1710, 2007.
- [48] R. Chester and T. D. Jickells, *Descriptive Oceanography: Water-Column Parameters*. John Wiley and Sons, Ltd, 2012, ch. 7, pp. 125–153.
- [49] *MC100 Underwater Optical Wireless Communication Modem*, 2020. [Online]. Available: <https://www.shimadzu.com/news/g16mjizzgbhz3-y.html>
- [50] M. Zhao, X. Li, X. Chen, Z. Tong, W. Lyu, Z. Zhang, and J. Xu, "Long-reach underwater wireless optical communication with relaxed link alignment enabled by optical combination and arrayed sensitive receivers," *Optics Express*, vol. 28, no. 23, pp. 34 450–34 460, 2020.
- [51] *B-Series Fast, Blue-Sensitive Silicon Photomultiplier Sensors datasheet*. SensL, 2013 (Rev. 3.1, Nov. 2015), available at <http://www.sensl.com/downloads/ds/DS-MicroBseries.pdf>.
- [52] M. Elamassie and M. Uysal, "Performance characterization of vertical underwater vlc links in the presence of turbulence," in *11th International Symposium on Communication Systems, Networks Digital Signal Processing (CSNDSP)*, 2018, pp. 1–6.
- [53] *Underwater Acoustic Positioning*. <https://www.advancednavigation.com/acoustic-navigation/>: Advanced Navigation, last accessed: 22 Dec. 2021.
- [54] M. Elamassie, M. Uysal, Y. Baykal, M. Abdallah, and K. Qaraq, "Effect of eddy diffusivity ratio on underwater optical scintillation index," *J. Opt. Soc. Am. A*, vol. 34, no. 11, pp. 1969–1973, 2017.
- [55] K. N. Fedorov, *The Thermohaline Finestructure of the Ocean: Pergamon Marine Series*. Elsevier, 2013, vol. 2.
- [56] T. Radko, *Double-diffusive convection*. Cambridge University Press, 2013.
- [57] E. Kunze, "A review of oceanic salt-fingering theory," *Progress in Oceanography*, vol. 56, no. 3-4, pp. 399–417, 2003.
- [58] I. S. Gradshteyn and I. M. Ryzhik, *Table of integrals, series, and products*. Academic press, 2014.
- [59] E. W. Ng and M. Geller, "A table of integrals of the error functions," *J. Res. Nat. Bur. Stand. Math. Sci.*, vol. 73B, no. 1, pp. 1–20, 1969.